



UPPSALA
UNIVERSITET

UPTEC Q 23012

Examensarbete 30 hp

Oktober 2023

Multifunctional ice and snow repellent coatings for photovoltaic modules

Gunnar Sandkvist

Civilingenjörsprogrammet i teknisk fysik med
materialvetenskap



UPPSALA
UNIVERSITET

Multifunctional ice and snow repellent coatings for photovoltaic modules

Gunnar Sandkvist

Abstract

Implementation of solar power by photovoltaic modules in cold climates, such as northern Sweden, implies several challenges. Ice and snow coverage not only leads to reduction in energy production due to shading, but it also puts equipment at risk from additional weight. The goal of this thesis was to formulate a passive ice shedding coating for photovoltaics that could handle the demands of both high optical transmittance and durability. In addition, the coating should be environmentally friendly and low cost. For that purpose, a state-of-the-art, superhydrophobic sol-gel silica-based coating was selected with the focus on optimizing its transparency, wettability, and durability. Different concentrations of binder, tetraethyl orthosilicate (TEOS), and catalyst (HCl) in the sol were explored, as well as post-treatment temperatures and sol aging. Hydrophobization was done by self-assembly of a silane and plasma polymerization of a siloxane. The coatings were characterized by UV-Vis spectroscopy, contact angle measurements, Scanning Electron Microscopy (SEM), X-ray Photoelectron Spectroscopy (XPS), tape peel strength, freeze-thaw cycling, ice adhesion force and a field test. Superhydrophobic, anti-reflective coatings with high transmittance ($88.5 \pm 1.9\%$) were achieved, with some of them retaining their superhydrophobic properties after 15 freeze-thaw cycles between room temperature and -20°C . The main findings were that the amount of TEOS in the sol has the largest influence on transmittance and strength, with more TEOS leading to less transparent but stronger coatings, and that calcination of the coatings greatly improves their durability.

Teknisk-naturvetenskapliga fakulteten

Uppsala universitet, Utgivningsort Uppsala/Visby

Handledare: Mikael Järn, Natalia Anna Wojas Ämnesgranskare: Jan Keller

Examinator: Lena Klintberg

Populärvetenskaplig sammanfattning

Elektrisk energi har varit avgörande för vetenskapliga landvinningar, teknologiska framsteg och välbefindandesutveckling de senaste 100 åren. Man har länge betraktat billig energi, inte bara elektrisk, som motorn i vår ekonomi. Idag talas det mer än någonsin om energieffektivisering och hållbarhet. Fossil energi och kärnkraft fasas ut i flera länder och koldioxidneutral har blivit ett ledord för många organisationer och företag. Trots detta minskar inte behovet av elektrisk energi, snarare kräver den gröna omställningen mer av det på grund av nya och växande industrier som fossilfri stålproduktion och batteritillverkning.

Ett sätt på vilket man kan alstra elektricitet är med hjälp av solceller. När ljus träffar en solcell omvandlas ljusets energi till elektrisk ström. Med solceller kan vi utvinna elektricitet så länge vår sol kommer att fortsätta lysa (åtskilliga miljarder år till), en praktiskt taget aldrig sinande källa till energi. Solceller kan sättas samman till paneler och monteras på byggnader eller på marken. Sverige har sitt nordliga läge till trots goda förutsättningar för solenergi – den mängd sol som infaller på en solpanel i vårt land är jämförbar med vad samma panel skulle fått i Mellaneuropa. Vårt kalla väder medför både fördelar och nackdelar för användningen av solceller. Fördelarna består i att omvandlingseffektiviteten ökar när solcellerna inte blir så varma. Det betyder att en större andel av energin från ljuset blir till elektrisk energi. En annan är att lägre temperaturer gör att anläggningarna kan hålla längre. Snö som ligger runt om solcellspaneler kan faktiskt bidra till att de producerar mer ström, då ljus effektivt reflekteras i den ljusa snön. Annars vad gäller snö och is, så är det till nackdel för solenergi. Även tunna snölager på paneler hindrar effektivt nästan allt ljus från att nå solcellerna, vilket gör att mängden energi som produceras minskar avsevärt. Snö, framför allt blötsnö, kan bli väldigt tungt och utgöra en risk för panelerna. Också smältning av is och snö som ansamlas kan leda till att vatten tränger in i utrustningen och skadar den. Delvis snötäckta paneler kan också utgöra en risk då det blir elektriska obalanser i dem. Att röja panelerna för hand är riskfyllt och inte alltid möjligt att utföras av privatpersoner som har solceller på sina tak. För företag med stora installationer innebär snöröjning en extra kostnad. Det finns också risk att panelerna skadas när de skottas av. Ett annat sätt att lösa nedisning är att värma panelerna med elektricitet men det är naturligtvis energikrävande.

Det har gjorts prov på att belägga solceller, eller snarare det glas som täcker dem, med tunna snö- och isavvisande skikt, med syftet att is och snö inte ska samlas på panelerna. En rad tekniker och material har studerats. Vissa skikt är släta, andra strukturerade på olika sätt. En del skikt innehåller till och med smörjmedel. Viktigt är att dessa skikt inte gör att ljusgenomsläppet till solcellerna minskar.

Ett sätt som studerats är så kallade superhydrofoba beläggningar. Hydrofob innebär vattenavvisande, och superhydrofob är alltså mycket vattenavvisande. Ett exempel på en superhydrofob yta är dagglåpanns blad som inte våts av vatten, utan vattnet bildar runda droppar som lätt rullar av bladen. Det har visat sig att vatten ofta inte ens hinner frysa till is på superhydrofoba ytor innan det rinner av och om is väl bildas på en sådan yta, sitter den väldigt löst och kan lätt falla av. Många sorters snö glider också lättare av superhydrofoba ytor än av glas. För att en yta ska kunna bli superhydrofob krävs två saker: rätt kemi och rätt ytstruktur. Med kemi menas att vissa molekyler har en tendens att repellera vatten. Med ytstruktur menas att ytan inte ska vara helt slät utan den behöver ha mikroskopiska håligheter i sig. En generell utmaning med denna typ av ytor är att uppnå tillräcklig nötningsstyrka. I och med att de har så små ytstrukturer skadas de lätt. En annan utmaning är att uppnå tillräcklig genomskinlighet. Särskilt svårt att kombinera bägge dessa egenskaper.

I detta examensarbete har det undersökts hur man kan optimera superhydrofoba ytbeläggningar på glas för användning i solceller i kalla klimat med snö och is. Beläggningarna har bestått av små partiklar kiseldioxid som bundits samman till en hård tunn film i en så kallad sol-gelprocess. Prov av glas har belagts genom att de doppats i lösningar. Efter doppningen har ytorna efterbehandlats genom att hettas upp i ugn i upptill 450°C. Dessa ytor är i utgångspunkten superhydrofila, d v s motsatsen till superhydrofoba, p g a kiseldioxiden de är tillverkade av. För att göra dem superhydrofoba har de hydrofoberats genom ytmodifiering med triklor(oktyl)silan (OTS). Recepten har varierats med avseende på koncentrationen av tetraetylsilikat (TEOS) och saltsyra (HCl), efterbehandlingstemperatur, åldring av lösningar och hur många gånger proven doppats. Även alternativa sätt att framställa ytorna har undersökts: dessa är (i) att skapa ett barriärskikt (SiO_x) i en plasmareaktor, (ii) att hydrofobera ytorna genom plasmapolymersering av hexametyldisiloxan (HMDSO) och (iii) att göra ytorna hydrofoba från början med en så kallad "one-pot"-metod.

För att karaktärisera ytbeläggningarna har det utförts en omfattande analys. Genom UV-Vis spektroskopi har den optiska transmittansen uppmätts. Kontaktvinkelmätningar av vattendroppar på ytbeläggningarna

har använts för att utvärdera vätningsegenskaperna. Kontaktvinklar har även uppmätts under daggpunkten för att ge information om ytbeläggningarnas förmåga att hantera kalla och fuktiga förhållanden. Genom att göra ett "tape-peel test" uppmättes ytskiktets styrka. För att avbilda ytorna i hög upplösning har svepelektronmikroskop (SEM) använts. Electron Spectroscopy for Chemical Analysis (ESCA), även kallat X-ray Photoelectron Spectroscopy (XPS), har utförts i syfte att mäta den kemiska sammansättningen på ytorna. Genom upprepad nedfrysning och upptining med dagg på proven (freeze-thaw cycling) har ytorna stresstestats i vinterlika förhållanden. Ett isvidhäftningsprov har utförts, där vatten fått frysa på ett prov där sedan den åtgående kraften för att avlägsna isen uppmätts, samt ett fälttest vintertid, där de snö- och isavvisande egenskaperna utvärderats.

Resultaten visar att det är möjligt med de metoder som använts att framställa superhydrofoba ytor som har högt genomsläpp av solljus, $88,5 \pm 1,9\%$ i genomsnitt, vilket är jämförbart med 90% för glas. Isvidhäftningen uppmättes till mellan 477 och 1670 gånger lägre än för glas. Fälttestet visade att ytorna fungerar som passiva snö- och isavvisande ytbeläggningar.

De främsta fynden är att den parameter som har störst inverkan på transmittans och styrka är koncentrationen av TEOS. Högre andel TEOS ger starkare ytor men lägre transmittans. Efterbehandlingstemperaturen har i huvudsak inverkan på ytornas styrka men också viss betydelse för ytornas vätningsegenskaper och deras transmittans.

Contents

1. INTRODUCTION	1
1.1 BACKGROUND	1
1.2 MOTIVATION	2
1.3 OUTLINE.....	2
2. THEORY	3
2.1 WETTING.....	3
2.1.1 Smooth surface.....	3
2.1.1.1 Young's relation.....	3
2.1.2 Rough surface	3
2.1.2.1 The Wenzel model.....	3
2.1.2.2 Cassie–Baxter model	4
2.1.3 Contact angle hysteresis.....	4
2.1.4 Relationship between wettability and contact angle hysteresis.....	5
2.2 ANTI-REFLECTIVITY	5
2.3 TECHNOLOGY OF THIN TRANSPARENT AR COATINGS	6
2.3.1 Sol-gel synthesis	6
2.3.2 Dip-coating application method.....	7
2.3.3 Plasma coating methods	7
2.3.4 Silane deposition	7
2.4 ICE AND SNOW ADHESION	7
2.5 TYPES OF PASSIVE ANTI-ICING COATINGS	8
2.5.1 Hydrophobic surfaces	8
2.5.2 Hydrophilic surfaces.....	8
2.5.3 Superhydrophobic surfaces.....	8
2.5.4 Slippery surfaces.....	9
3. MATERIALS AND METHODS	11
3.1 METHODS FOR COATING DEVELOPMENT.....	11
3.1.1 Substrate preparation.....	11
3.1.2 Formulations	11
3.1.3 Coating process	12
3.1.4 Plasma polymerization.....	13
3.2 SURFACE CHARACTERIZATION METHODS.....	13
3.2.1 Optical transmittance.....	14
3.2.2 Surface wettability.....	14
3.2.3 Freeze-thaw cycling	14
3.2.4 SEM imaging	15
3.2.5 Surface profilometry	15
3.2.6 Surface elemental analysis by X-ray Photoelectron Spectroscopy	15
3.2.7 Tape peel testing	16
3.2.8 Ice adhesion	16
3.2.9 Field test for snow and ice shedding evaluation	17
4. RESULTS AND DISCUSSION	18
4.1 CHEMICAL ANALYSIS	18
4.2 OPTICAL TRANSMITTANCE AND COATING THICKNESS	18
4.3 WETTING.....	20
4.4 TAPE PEEL RESULTS.....	23
4.5 FREEZING RESILIENCE	25
4.6 ICE ADHESION RESULTS.....	27
4.7 RESULTS FROM FIELD TEST	28
5. CONCLUSIONS.....	30
6. FUTURE WORK	32
7. ACKNOWLEDGEMENTS	33
8. REFERENCES.....	34
9. APPENDICES	38
APPENDIX A – SAMPLE NOMENCLATURE	38
APPENDIX B – PROFILOMETRY PLOTS	39
APPENDIX C – TABLES.....	41

Abbreviations and symbols

AR	Anti-reflective
ARF	Adhesion reduction factor
CA	Contact angle
CAH	Contact angle hysteresis
DMDEOS	Dimethoxydimethylsilane
FTC	Freeze-thaw cycles
FTS	Freeze-thaw survival
HMDSO	Hexamethyldisiloxane
HP	Hydrophobization
IPA	Isopropyl alcohol
LBL	Layer-by-layer deposition
LWC	Liquid water content
MCT	Medium-chain triglyceride
OTS	Octyltrichlorosilane
PDMS	Polydimethylsiloxane
PMVS	Polymethylvinylsiloxane
PV	Photovoltaic
RA	Roll-off angle
RADP	Roll-off angle at dewpoint
RH	Relative humidity
RT	Room temperature
SAM	Self-assembled monolayer
SEM	Scanning electron microscopy
SH	Superhydrophobic
SiO _x	Glass like Silicon oxide
SLIPS	Slippery Liquid Infused Porous Surface
TSW	Solar weighted transmittance spectrum
TEOS	Tetraethyl orthosilicate
TPCL	Three phase contact line
VF40	VytaFlex 40, a polyurethane rubber
WCA	Static water contact angle
XPS	X-ray photoelectron spectroscopy
α	Contact angle hysteresis
γ	Surface tension / Surface energy
θ	Contact angle
λ	Wavelength

1. Introduction

1.1 Background

Solar cells are an important means to produce green electricity for the future and help reducing greenhouse gas emissions. Even in colder climates, solar energy can give an important contribution to the energy mix and in Sweden photovoltaic (PV) installed capacity is growing at an exponential rate, see Figure 1. However, with 2 TWh produced in Sweden in 2022, solar still made a contribution of not more than about 1% of the total energy production¹.

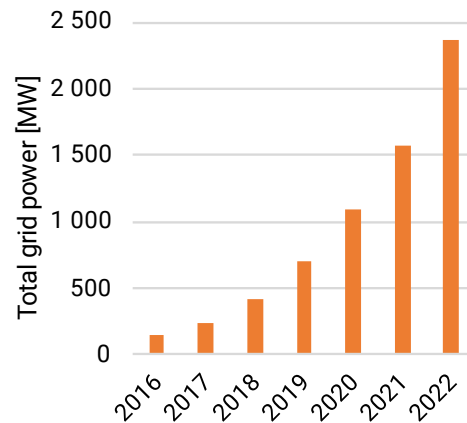


Figure 1: Total power from solar cell installations connected to the power grid in Sweden. Source Swedish Energy Agency².

Despite higher latitudes, solar flux is not inconsiderable, especially during the summer months but also in early fall and late winter. Looking at annual solar irradiation, the difference between a central European location such as Munich at 48° latitude and a location in northern Scandinavia such as Piteå at 65° is only about 10%³. Moreover, cooler weather increases efficiency of the cells and reflections from snow covered surroundings can make considerable contributions, since freshly fallen snow has an albedo of up to 90%, while spring snow has an albedo of around 60%³. Figure 2 shows global annual snow cover duration. Large parts of the industrialized world, North America, Europe, and Asia, have snow cover a significant part of the year.

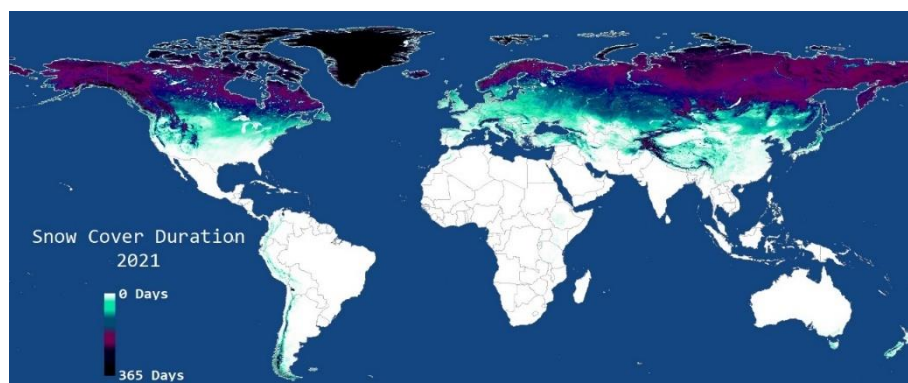


Figure 2: Duration of snow cover during the 2020/2021 hydrologic year (1 Sept. 2020 – 31 Aug. 2021). Figure and caption are reprinted from⁴.

There are, however, a few things to consider when installing solar cells in colder climates that are related to ice and snow buildup on the panels, as well as the nature of irradiation at higher latitudes, that on average is more diffuse³. At 2 centimetres of snow coverage on solar cells, 80% of the incident light will be blocked from reaching the panel⁵, and although the cold season is the least productive, the annual production can be reduced by up to 20% when panels are covered by snow in the winter⁶. More importantly, it has been shown that while uniform shading of a PV system merely reduces output, partial shading may cause

complex changes of the electrical behaviour of the solar cells, potentially damaging it⁷. Snow accumulation also puts mechanical load on panels and rooftops and melting can lead to damage of installation, both mechanical and electrical⁷. Manually removing ice and snow is hazardous, costly and can wear or even damage the solar cells^{7,8}. Snow and ice mitigation techniques include heating the solar cells, either by separate coils or by running current through the solar cells by a reversible converter⁷. That would demand electricity and add complexity, however. The angle at which the panels are mounted will affect how easily water, snow and ice slide off, and can be optimized regarding solar flux, although many times the panel orientation is constrained by building geometry⁸. Some work has been done exploring passive methods for keeping solar panels clear from snow and ice⁹. Snow and ice repellency is linked to water repellency^{9–11}, thus a superhydrophobic (i.e. strongly water repellent) coating of the solar panel may be a solution, if a coating can be found that is sufficiently transparent, preferably anti-reflective (AR), and durable enough. However, the durability of porous superhydrophobic coatings remains a big challenge^{12–14}.

1.2 Motivation

The aim of this master thesis was to improve on or find new solutions regarding passive coatings for solar panels with enhanced energy production and reduced maintenance need in colder climates.

Requirements of a passive coating:

- a) **Increased optical transmittance**
The coating should ideally increase the optical transmittance of the cover glass of the PV module, or at least not worsen it. The annual production should not decrease compared to uncoated cover glass.
- b) **Durable, environmentally friendly, and scalable**
The coating should be easily applied in a scaled-up process. It should be durable and possible to reapply if necessary. The coatings should withstand exposure to radiation (UV), temperature cycles, freezing, thawing, heavy rain and hail, ice, snow, and wind. The coating should not be harmful to the environment. For instance, fluorocarbons should be avoided.
- c) **Ice- and snowphobic**
The coating should repel ice and snow and avoid dust build-up. Ice should either not build up because of water repellence, or the ice adhesion to the coating should be low enough to allow for the ice to fall off before becoming too thick and thus detrimental to transparency and causing damage to the PV modules. Because of the significant reduction of the power output and the hazards both mechanically and to the electrical systems from snow cover on solar panels, the surface coating should also facilitate passive snow removal.

1.3 Outline

In this master thesis, the aim was to develop a range of functional superhydrophobic coatings of high durability, and good optical properties, to be used on the cover glass of solar cell panels. The report is structured in a following manner. In the first part of the thesis, the theoretical aspects regarding essential wetting and optical properties of surfaces are discussed. A short description of relevant methods for manufacturing of thin transparent coatings is given, with an emphasis on sol-gel based technologies that are in focus of this work. A review of the state-of-the-art regarding anti-icing and anti-snow coatings is also included in the Theory section. In the Materials and Methods section, a description of the explored coating manufacturing processes is presented, together with an overview of the surface characterization techniques that were utilized to evaluate developed materials. In the Results and Discussion section the most significant results are presented. The most important findings are finally summarized in the Conclusions section with remarks on possible next steps in the Future work.

2. Theory

2.1 Wetting

Wetting, the phenomenon where a liquid is spread over a solid surface (or an immiscible liquid phase), is driven by the respective interphase surface energies¹⁵. Atoms and molecules within a bulk or a liquid tend to have lower free energy than those on a surface. In a three-phase system, a liquid, a solid and a gas will have three surface energies here denoted γ_{SL} for the solid – liquid interface, γ_{SG} for the solid – gas interface and γ_{LG} for the liquid – gas interface. The degree of spreading of a liquid on a solid is defined by the magnitude of these interfacial energies – or in other words, wetting will occur when the free energy of the system decreases¹⁶.

2.1.1 Smooth surface

When a drop of liquid is formed on an ideal, smooth solid surface, the contact angle (CA) will be a three-phase boundary point. The contact angle, θ_Y is defined as the angle between the tangent to the liquid-vapour-interface and the tangent to the solid interface at the contact line between the three phases¹⁶. This is illustrated in Figure 3 where the three-phase contact line (TPCL) is marked by the red circles. In Figure 3(a) the solid surface is hydrophobic with $\theta_Y > 90^\circ$ while in Figure 3(b) the solid surface is hydrophilic, with $\theta_Y < 90^\circ$.

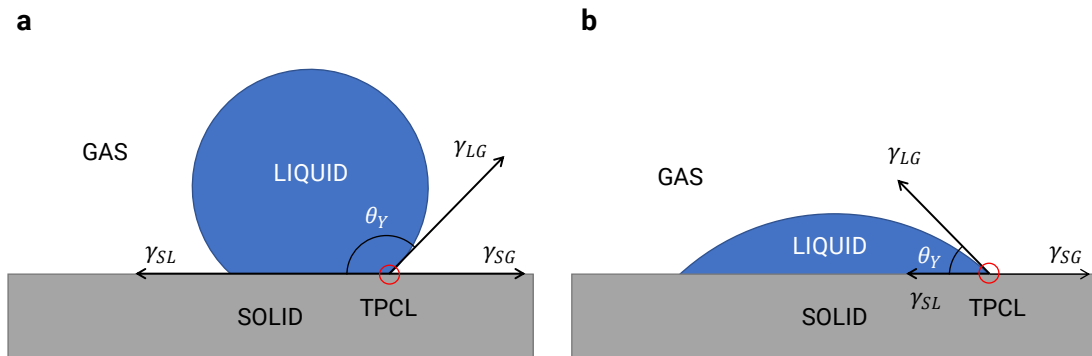


Figure 3: Contact angle definition. (a) shows a hydrophobic surface with CA $> 90^\circ$ while (b) shows a hydrophilic surface with CA $< 90^\circ$.

2.1.1.1 Young's relation

For an ideal, smooth, and chemically homogenous surface the contact angle can be described by Young's relation (Eq. 1) after Thomas Young:

$$\gamma_{SG} = \gamma_{LG} \cos \theta_Y + \gamma_{SL} \quad (1)$$

If γ_{SL} is large compared to γ_{SG} , the CA will be large as shown in in Figure 3(a). In the opposite case, if γ_{SL} is small compared to γ_{SG} , the liquid will wet a large patch of the solid's surface as illustrated in Figure 3(b). It is important to note that the solid-liquid-gas system is characterized by a single θ_Y , since the Gibbs energy vs contact angle curve for an ideal solid-liquid gas system has only one minimum¹⁷.

2.1.2 Rough surface

Real surfaces are neither perfectly smooth nor chemically homogenous. For microscopically (nano- or even molecular scale) rough surfaces, wetting behaves differently than in the ideal case. Thus, Young's equation (Eq. 1) is not applicable to such surfaces. To account for surface roughness, there are two basic models that commonly are used to explain CA¹⁷, depending on structure, scale and wetting mechanism.

2.1.2.1 The Wenzel model

In the Wenzel model, after Robert N. Wenzel, the liquid is assumed to wet all the pits and groves and the surface, see Figure 4(a). The apparent contact angle θ_W , that is the macroscopic contact angle measured when disregarding microscopic surface features, is related to θ_Y by the relation:

$$\cos \theta_W = r \cos \theta_Y \quad (2)$$

where r is a roughness factor being the quotient between the real surface area and the projected surface area¹⁸. Thus, the equation implies that for a rough hydrophilic surface ($\theta_Y < 90^\circ$), θ_W will be greater than θ_Y . That is, it will seem more hydrophilic than a smooth surface with the same chemical composition. Likewise, a rough hydrophobic surface ($\theta_Y > 90^\circ$) should appear more hydrophobic than a smooth surface having the same chemical composition¹⁸.

2.1.2.2 Cassie–Baxter model

When the surface asperities are narrow enough, a drop will stay on top, trapping gas below. For such a case the Cassie – Baxter model gives the following description:

$$\cos \theta_{CB} = -1 + f_s (\cos \theta_s + 1) \quad (3)$$

where f_s is the fraction of solid material and θ_s is the intrinsic CA for the solid material on a smooth surface, similar to θ_Y ¹⁸. The explanation for Eq. 3 is that the prerequisite for trapping air is that the local contact angle is larger than 90° .

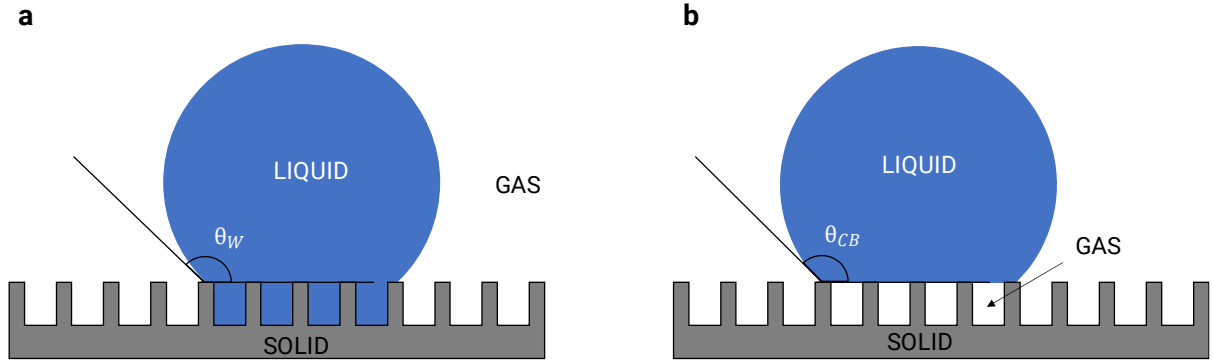


Figure 4: (a) Wenzel model and (b) Cassie-Baxter model of wetting. In the Wenzel model the liquid is assumed to penetrate the structure completely whereas in the Cassie-Baxter model, the liquid droplet is assumed to sit on top of asperities, effectively leaving air pockets beneath it.

2.1.3 Contact angle hysteresis

The models for contact angles described here: Young's, Wenzel and Cassie-Baxter all assume a drop resting on a surface in equilibrium. Real surfaces, that to some extents are rough or chemically heterogeneous, can exhibit a range of contact angles, defined as contact angle hysteresis. There has been some debate on the validity of both the Wenzel and Cassie-Baxter equations¹⁹. The ability to predict the apparent static contact angle by interactions at the three-phase contact line rather than by interactions below the droplet has been underlined^{19,20}. In fact, the Wenzel and Cassie-Baxter equations has been disproven in experimental work with the purpose of testing their validity^{21,22}. More recent studies however, have shown that the Wenzel and Cassie-Baxter equations indeed are valid as approximations for contact angle and that their validity increases as the scale of the heterogeneities decreases relative to the droplet size²³. Contact angle hysteresis (CAH) can be determined by either increasing or decreasing the volume of a drop, as depicted in Figure 5(a), where the advancing contact angle, θ_{adv} , is the maximum CA found when pumping up a drop and the receding contact angle, θ_{rec} is the minimum CA when emptying the same drop. CAH is an angle and is defined as θ_{hys} :

$$\theta_{hys} = \theta_{adv} - \theta_{rec} \quad (4)$$

An alternative method to determine CAH is by the tilted drop method. Here θ_{adv} and θ_{rec} are found by tilting the surface the drop is applied on and measuring CA on both sides of the drop, see Figure 5(b). For the tilted drop method, Eq. 4 still applies.

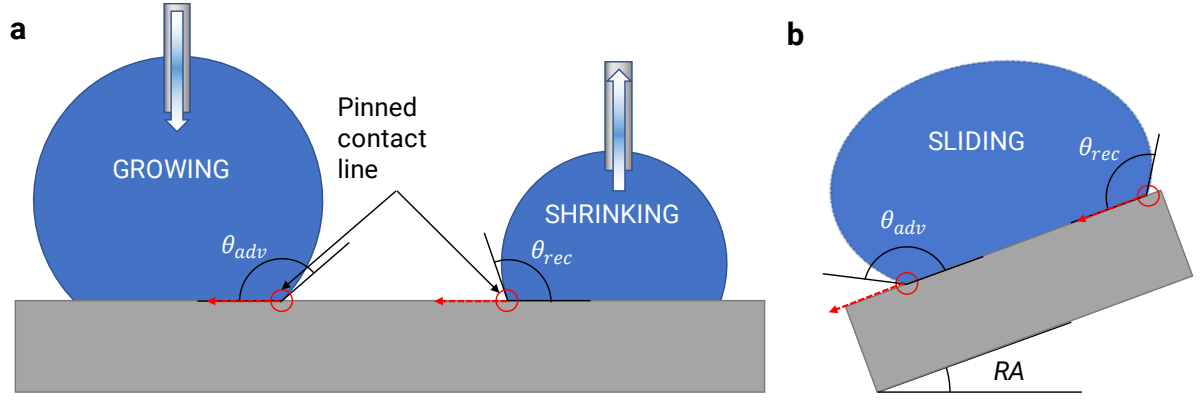


Figure 5: Two ways of determining contact angle hysteresis. (a) is by the sessile drop method and (b) is by tilted drop method. The red arrows indicate the direction of movement of the contact line.

The origins of CAH are caused by chemical heterogeneities and/or roughness. Even perfect surfaces will in most cases have some CAH¹⁸. Also surfaces with a high static CA still can have a high CAH. This means that drops of water tend to stay on a spot when subjected to external forces. If the aim is to have a surface that easily repels water, then CAH should be as low as possible^{18,24}.

2.1.4 Relationship between wettability and contact angle hysteresis

A surface's (water) wetting behaviour can be described by its water contact angle (WCA) in either one of three categories. Hydrophilic surfaces have $WCA < 90^\circ$, hydrophobic surfaces have a $WCA > 90^\circ$ and superhydrophobic (SH) surfaces have $WCA > 150^\circ$. However, about 120° is the known native limit for a smooth surface^{12,18}. To reach higher contact angles, the surface must not only be chemically hydrophobic, that is have a low surface energy, but also have a certain roughness. If the dimensions of the structure of the surface is considerably smaller than a drop of water sitting on it, the Cassie-Baxter case discussed in 2.1.2.2 can be obtained. Especially hierarchical (roughness on several length scales) micro- and nanostructures have been shown to be key¹⁸ and can yield very high WCA above 175° ²⁵. Several groups have pointed out that the static contact angle is insufficient to give a full description of a surface's wettability. One such argument is that there is not a one-to-one correspondence between the static contact angle and when a droplet slides off a surface^{26,27}. Furmidge²⁸ suggested an equation predicting when a droplet should slide off a surface

$$(mg/w)\sin(\alpha) = \gamma_{LG}(\cos \theta_{rec} - \cos \theta_{adv}) \quad (5)$$

where m is the mass of the drop, g is the gravitational constant and w is the projected width of the drop perpendicular to the sliding direction. Only advancing and receding contact angles, not the static contact angle, will correlate with α in Eq. 5. Thus, for a surface to be truly superhydrophobic, it must have a low CAH in addition to high WCA. If there is a transition from a Cassie-Baxter state to a Wenzel state, water drops on a SH surface will become pinned and unable to slide off easily. Hierarchical surface morphologies tend to lower transition energies and hence show lower CAH¹⁸.

2.2 Anti-reflectivity

When light passes from one medium to another, at the interface, some of that light will reflect into the first medium, given the media have different refractive indices. Refractive index, usually denoted by n , is an intrinsic property of materials and is inversely proportional to the materials light speed (phase speed). That means, for example that air has n close to 1 and glass 1.5²⁹. The phenomenon of interfacial reflection is called Fresnel reflections. In the simple case, when light hits perpendicular to the interface, the reflectance R can be written as

$$R = \left(\frac{n_2 - n_1}{n_2 + n_1} \right)^2 \quad (6)$$

where n_1 and n_2 are the refractive indices of the two materials²⁹. Of the light passing through the interface, some of it will be absorbed in the entered medium and the remainder will be transmitted through it. Due to the law of energy conservation, we have the relation:

$$T + A + R = 1 \quad (7)$$

where T for transmittance denotes the amount of transmitted light²⁹. A and R are assigned to the corresponding quantities absorbance and reflectance. Eq. 7 tells us that less reflectance will give us more transmittance, assuming absorbance is constant. Moreover, R is also dependent on the incident angle, where a shallower angle will result in higher reflectance. For many applications, A can be ignored, and we can consider $T = 1 - R$. In other words, R must be decreased to improve transmittance.

There are several methods to reduce R by introducing a material to the interface, a so-called anti-reflective coating. The perhaps simplest way is to use a thin layer of dielectric with $n_1 < n < n_2$. When n and the layer thickness d are carefully tuned, destructive interference will occur and as a result R will decrease. In fact,

$$d = k \frac{\lambda}{4n} \quad (8)$$

and

$$n = \sqrt{n_1 n_2} \quad (9)$$

where λ is the wavelength of the incident light and k is a positive integer will give the most reflectance reduction³⁰. Assuming $n_1 = n_{\text{air}} = 1$ and $n_2 = n_{\text{glass}} = 1.5$, we can see that the optimal n for a single layer AR coating would be 1.22. The desired thickness of the film will depend on the targeted transmission peak, since a distribution of photons with wavelengths in the range of 300-1100 nm will be used for conversion to electricity. Zäll et al.³¹ aimed for a film thickness of 120 nm. It may be challenging to find materials with optimal n . Effective Medium Theory (EMT) can be applied if the material of the medium is inhomogeneous, and the granularity is appreciably smaller than λ . In that case an effective refractive index n_{eff} can be considered a volume weighted average of its constituents. Being a simplification, volume averaging theory (VAT) shows good agreement with numerical finite element method simulations. A porous material can thus have its n_{eff} lower than the bulk³¹.

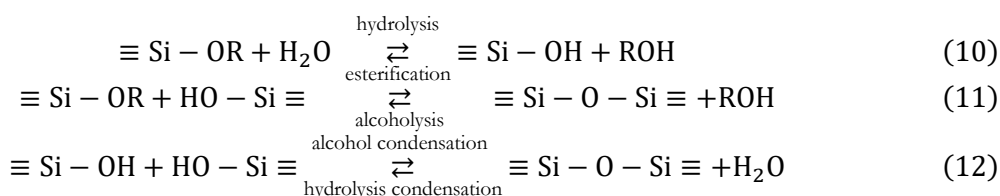
2.3 Technology of thin transparent AR coatings

Thin, transparent coatings can according to a review by Shanmuga et al.³² be manufactured by a range of different materials and techniques, and the latter can be divided into conventional and unconventional techniques. For the conventional techniques, there are top-down and bottom-up approaches. Top-down techniques remove material from a substrate, usually by etching. Bottom-up techniques add material to a substrate. Top-down methods involve techniques such as lithography, template-based methods, and plasma treatments to modify the surface. In contrast, bottom-up approaches involve self-assembly and self-organization techniques, including chemical deposition, layer-by-layer deposition (LBL), and colloidal assemblies. Some techniques combine top-down and bottom-up approaches, such as casting of polymer solutions, phase separation, and electrospinning^{12,14,25,33–37}. Top-down techniques such as lithography have the advantage of good control of morphology and structure of the surface. Compared to bottom-up approaches, the strength is also better in general, as there is no interface between substrate and coating with potential adhesion issues. Sol-gel, one bottom-up method, is industrially used to produce AR coatings, and has the advantages of being inexpensive, simple, and fast³². AR coatings can be made by Silicon dioxide (Silica) and sol-gel, which have the advantages being stable, having low refractive index and inexpensive. By using dip-coating, that is dipping substrates in solutions, Mahadik et al. Reached transmittance of 97.5% at 500 nm wavelength from a single layer silica coating. That was possible due to the porosity and optimized thickness of the coating³⁸.

2.3.1 Sol-gel synthesis

Sol-gel chemistry is a method used to prepare nanomaterials with organized structures on the nanometre scale. The “sol” in sol-gel is a colloidal suspension of solid particles that acts as a precursor for a network (the “gel”) of discrete particles or network polymers. Sol-gel chemistry can be carried out at room

temperature and is widely used in various industrial applications. The process starts with stable sols and can produce inorganic fibres, thin films, powders, and bulk materials with homogeneous pore structures. Both organic and inorganic precursor molecules can be used in the process. Silica is the most frequently used sol-gel system, and silica gels are typically synthesized by hydrolysing tetrafunctional alkoxide precursors using a catalyst. The sol-gel process involves three equilibrium reactions – hydrolysis (Eq. 10), alcohol condensation (Eq. 11) and water condensation (Eq. 12) – that produce siloxane bonds with alcohol and water as by-products. R is an alkyl group. The relative kinetics of these reactions are determined by various parameters, including the type of precursor, pH of the sol, H₂O/Si molar ratio, temperature, co-solvents, and solubility of silica, which can affect the morphology of the final product³⁹.



2.3.2 Dip-coating application method

There are several ways to apply a sol to a substrate. Common methods are spray coating, dip-coating, and spin-coating. While spin-coating gives precise thickness, it is not well suited for larger surfaces such as solar panels. Dip-coating provides great control of the film thickness while it also produces homogenous films. The solution can also be reused until depletion or evaporation, making it a good choice for industrial applications¹⁶. With dip-coating, the substrate is immersed in the solution with precursors and withdrawn upwards at a controlled speed. According to Faustini et al.⁴⁰, the relation between pull-up rate and film thickness can be divided into three separate regimes. The first is the draining/evaporation regime described by the Landau – Levich model, for which faster pull-up rates give thicker films. The second is the capillary/evaporation regime, for which slower pull-up rates give thicker films, since evaporation of the solvent is fast relative to the sample movement upwards. They also found a mixed draining/capillary/evaporation regime for intermediate speeds, for which the film thickness can be perfectly described as a superposition of the previous two regimes. Other than pull-up speed, concentration, surface tension and viscosity of the sol will affect the coating thickness⁴⁰.

2.3.3 Plasma coating methods

The term plasma, introduced by Langmuir in 1928, is ionized gas and is considered the fourth state of matter^{41,42}. Ions, electrons, radicals as well as molecules and neutrals can coexist in a plasma. A plasma can be created by energizing a gas, or a mixture of gases such as air, for instance by heating it or by applying an electric field to it. Common plasma discharge types are direct current (DC) and radio frequency discharge plasmas (RF). Since electrons are much lighter than ions, the electron temperature can be very high (typically >5000K) while heavier particles such as atoms and ions stay relatively cold. Consequently, plasma methods can be very useful for treating temperature sensitive materials⁴³.

2.3.4 Silane deposition

Organosilicon molecules, or commonly silanes, are commonly used for functionalizing surfaces in a process called silanization. The silane group (trichloro, trimethoxy or triethoxy) reacts with OH-groups on the surface through self-assembly, creating a self-assembled monolayer (SAM), and can be deposited as liquid or from vapour phase. The end group can have lots of different functional groups and properties, and thus can render a surface hydrophobic or hydrophilic⁴⁴.

2.4 Ice and snow adhesion

Determining the ice and snow adhesion to a solid surface is complex because of the multitude of accretion mechanisms and the different morphologies of snow and ice⁴⁵. Makkonen et al. have laid out the theoretical aspects of ice adhesion, generally given as F/A , where F is the force required to remove the ice from a surface area A ⁴⁶. Testing can be done by centrifuge tests, direct mechanical tests and miscellaneous tests. Examples of the latter include tension tests, pre-cracked tension, torsioned beam, tensioned beam, four-point beam, laser spallation and vibrating beam⁴⁷. Due to the multitude of measuring methods for ice adhesion, comparison of results can be difficult. There are however attempts to compare different methods

and to develop standards^{48,49}. Recently, the effects of different types of ice on ice adhesion strength have been studied⁵⁰. Ice adhesion strength of precipitated ice (hard rime), in-cloud ice (impact ice) and bulk water ice (clear ice) was compared on aluminium substrates in a centrifugal ice adhesion test. The findings suggest that the strength of ice adhesion decreases as the ice density increases, with the weakest adhesion seen in clear ice and the strongest in hard rime ice. It seems that the stiffness and porosity of ice have an unforeseen impact on ice adhesion strength, and further research is necessary to understand how the icing process influences the mechanisms of adhesion. Meuler et al. studied the relationship between water wettability and ice adhesion and found a good relationship between the ice adhesion and the work of adhesion, the surface tension and the receding contact angle⁵¹. However, it is important to stress that the relationship is valid only for smooth surfaces. For structured surfaces, ice can penetrate the structure depending on the ice accretion mechanism, and the relationship may no longer be valid.

While ice adhesion on different types of surfaces have been extensively researched, there are much fewer studies on snow adhesion. Anderson et al. reviewed passive snow repulsion of coatings, and concluded that the amount of studies is very limited⁵². However, Kako et al. found that superhydrophobic surfaces reduces adhesion of both wet and dry snow and facilitates sliding of dry snow⁵³. They also found that wet snow slides easier on hydrophilic surfaces. This behaviour was explained by the presence of a water film on hydrophilic surfaces that acts as a lubricating layer, while the superhydrophobic surface rejects the water film and leaves the snow crystals in contact with the dry surface and thus hindering the sliding behaviour.

2.5 Types of passive anti-icing coatings

There are three commonly seen approaches to icephobicity. These are: (i) to prevent frost formation from humid air by denying ice nucleation, (ii) delaying the ice nucleation to allow for water to shed before ice formation, and (iii) reducing the ice adhesion to allow for easy shedding of ice that is formed. Since ice can form in several ways (rime, frost, and glaze) one technology is not necessarily best in all cases⁸. Several passive means of ice mitigation have been examined, and state-of-the-art is described in the review by Kreder et al.⁹. Ice prevention by surface engineering of PV modules was presented in a review by Fillion et al.⁵⁴.

2.5.1 Hydrophobic surfaces

One way of achieving an ice-repellent surface is by applying a hydrophobic coating to it. Surfaces that are hydrophobic have contact angles exceeding 90°. CAH should be low to facilitate ice sliding of and that is typically achieved if the surface is smooth and defect free. Meuler et al. used a broad range of commercial polymers to prepare water repellent surfaces to verify that there is a linear relation between $1 + \cos \theta_{rec}$ and ice adhesion⁵¹. A general advantage with hydrophobic surfaces is that they are durable since they are smooth. A drawback is that their performance is lower than state-of-the-art because of their relatively high ice adhesion compared to other technologies such as superhydrophobic surfaces⁹.

2.5.2 Hydrophilic surfaces

While ice adhesion is high on hydrophilic surfaces and hydrophilic coatings are not generally considered as anti-icing, they have a few features that in certain circumstances can make them attractive for such purpose. One is that nanostructured hydrophilic surfaces have a longer ice nucleation delay times than hydrophobic surfaces, and according to Jung et al. surfaces with minimal roughness of 1.4-6.0 nm having the longest freezing-delay times⁵⁵. That means, ice will not form at all on such surfaces. Another notable characteristic of hydrophilic surfaces is that since water tends to spread out evenly, ice nucleating from it will form a smooth layer and not diffuse light. It may also be argued that a smoother ice layer let snow slide off easier, should there be subsequent snowfall after ice formation⁹. The biggest advantages with hydrophilic surfaces are their commercial availability and that they are durable. However, their anti-icing properties are not as good as other types of ice-phobic coatings.

2.5.3 Superhydrophobic surfaces

Superhydrophobic coatings have shown promising properties as anti-icing coatings in a number of studies^{52,53,56-58}. Thanks to their low contact angle hysteresis and self-cleaning properties, ice formation is prevented since water from rain readily slides or bounces off before ice formation⁹. Another advantage with SH surfaces is that they, likely due to reduced heat transfer between the surface and the liquid because of the small contact area, freezing of droplets is delayed, giving them more time to slide off the surface before ice is formed. One thing to consider is that the surface must prevent a raindrop hitting at terminal

velocity from entering, otherwise the water may wet the surface in the Wenzel state. If ice still forms on SH surfaces, the ice-adhesion is low, facilitating the ice to slide off. Silica based SH coatings can readily be made using sol-gel methods. Gao et al. prepared superhydrophobic films by dip-coating glass substrates in silica sols. A water contact angle $>150^\circ$ and sliding angle $<5^\circ$ was achieved for a film dipped into silica sols of 10 nm particles, 25 nm particles and mesoporous particles (45 nm), respectively⁵⁹. Another approach to a highly transparent superhydrophobic coating was used by Manca et al.¹². The coating was prepared in two steps by first applying a dense organosilica layer and the nanoparticle-based hydrophobic layer in the second step. The coating exhibited strong water-repellent properties in conjunction with a maximum transmittance of 93.5%. Durability of superhydrophobic coatings remain a challenge though – the nanostructures of superhydrophobic coatings can easily be damaged, and then the superhydrophobic property is lost. Another challenge is to resist water vapour condensing into the surface structure, leading to a Cassie-Baxter to Wenzel transition in wetting state⁶⁰.

2.5.4 Slippery surfaces

One approach to produce non-stick surfaces is having lubrication liquid locked into a porous structure. Slippery Liquid Infused Porous Surfaces, or SLIPS⁶¹, employs a lubrication liquid layer to achieve low ice adhesion, excellent frost repulsion, and reduced freezing time⁶². Figure 6(a) illustrates the concept. The lubricant will form a thin lubricating layer between the surface and any ice, significantly reducing adhesion and shear force to remove the ice. Softer surfaces seem to initiate crack propagation in ice so that for larger surfaces, less force than the *nominal area* \times *maximum shear stress* is needed for ice shedding⁶³.

Different variations of SLIPS have emerged using varying approaches. Rykaczewski et al. used a microstructured surface combined with a perfluorinated oil and tested it for frost repulsion⁶⁴. However, they found that the oil responsible for the surface's icephobic properties was depleted within a single frosting cycle due to different surface energies leading to the oil wetting frozen droplets. Shedding these droplets removed some of the lubricant, ultimately leading to a loss of icephobicity. Other lubricants than perfluorinated oils have also been explored, such as organosilicon compounds, vegetable oils, mineral oils, and hydrocarbons.

There are commercial options utilizing the concept such as LiquiGlide and Adaptive Surface Technologies. A related approach to SLIPS with the aim of improving the durability of the coating by delaying lubricant depletion, is to infuse an elastomer with a lubricant, with the elastomer matrix serving as a reservoir, see Figure 6(b). For example, Zhu et al. infused Polydimethylsiloxane (PDMS) and Yeong et al. infused a commercial polymer (SilprocoatTM) with silicon oil to repeatedly achieve low ice adhesion^{65,66}. PDMS coatings incorporated with paraffin by Zhuo et al. was shown to be able to regenerate lubricant to the surface⁶³. Tao et al. infused fluorinated PMDS with and polymethylvinylsiloxane (PMVS) as lubricant⁶⁷. Golovin et al. Infused VytaFlex 40 (VF40) with medium-chain triglyceride oil (MCT) to achieve a coating with an ice adhesion of 4.9 kPa⁶⁸.

One intriguing method involved a combination of tetraethyl orthosilicate (TEOS) and dimethoxydimethylsilane (DMDEOS) in a PDMS matrix. This combination, as reported by the authors, led to the creation of remarkably smooth films with a high degree of mobility within the PDMS chains⁶⁹. These films displayed minimal sliding angles for both water and hexadecane, and their transmittance was 2-4% greater than that of untreated glass. SLIPS are promising as anti-icing coatings because of their low CAH and low ice-adhesion. However, they are prone to lubricant depletion and the structured surfaces may be wear sensitive. Liquid-infused elastomers show extremely low ice adhesion and can readily be formulated into commercial polymeric systems. Their drawbacks are that there are still as of time of writing no commercial coatings on the market and, since their novelty, long term durability is an unknown.

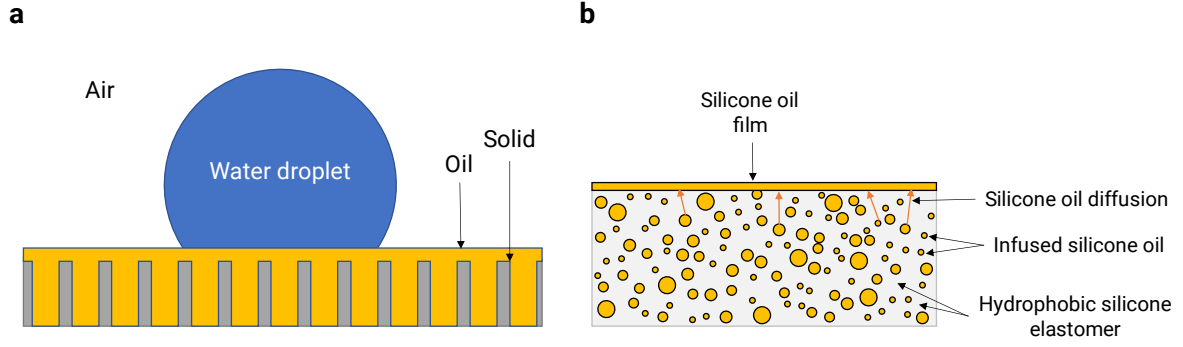


Figure 6: (a) SLIPS principle. Mesoporous structure filled with silicone oil. (b) Elastomer infused with silicone oil. Both will provide a liquid oil film on top of the coating.

In a recent publication by Dhyani et al., researchers applied icephobic lubricant infused elastomer coatings to solar cells and conducted field tests in Alaska⁵⁷. The coatings tested on the solar panels consisted of PVC + 60 wt% MCT oil (MC2) and PDMS (MC6), respectively. The authors claimed an increase in energy yield of up to 80% for the coated panels compared to the uncoated ones. However, due to the relatively large thickness of the coatings, their optical characteristics were not outstanding. The transparency of the MC2 coating (approximately 5 μm thick) was lower than that of uncoated glass, while the MC6 coating (45-50 μm thick) fell within the range of glass transparency.

3. Materials and methods

3.1 Methods for coating development

In this section the methods of preparing the samples and the sol formulations are described as well as the coating processes, both by dip-coating and by plasma polymerization techniques. The photovoltaic cells on commercial solar panels are covered by a protective glass. Either the PV module itself or the cover glass is usually AR treated in some way to increase panel efficiency³². Therefore, in this thesis project, the coating development was done on glass, as if the coatings would be applied on a cover glass for solar cells. We chose a sol-gel synthesis route and varied parameters like the TEOS content, post-treatment temperature, amount of HCl and sol aging.

3.1.1 Substrate preparation

In the development of the multifunctional snow and ice repellent coatings, the substrates used were either low iron float glass (Pilkington) or silicon wafers. The reasons for that are that a coating would go on top of the cover glass of the solar cells, and silicon wafers were used for Scanning Electron Microscopy (SEM) and X-ray Photoelectron Spectroscopy (XPS) characterizations. The samples were cut into 25x50 mm pieces and cleaned with isopropyl alcohol (IPA) and rinsed with laboratory grade ethanol and Milli-Q Type 1 water and dried with compressed air. Samples intended for XPS and SEM analysis were cut into smaller pieces, 8x25 mm. Just prior to dip-coating, the substrates were air plasma cleaned for 2 minutes in a Harrick PDC-32G at RF level on the highest setting, 18 W. The plasma cleaning also activated the surfaces for better adhesion between the coatings and the substrates.

3.1.2 Formulations

The superhydrophobic coatings were prepared by adding fumed silica (Sigma-Aldrich, 14 nm primary particle size) to analytical grade ethanol (Solveco) and disperse in an ultrasonic bath (Elma Transsonic digital) at highest power for 30 minutes at room temperature. Further dispersion was done by sonicating with a probe sonicator (Vibracell) at 20 kHz frequency at 300 W power for 5 minutes sonicating time, pulse intervals 40 seconds on and 20 seconds off to prevent excessive heating. Tetraethyl orthosilicate (TEOS), (Sigma-Aldrich 97%) and HCl were added and stirred for at least one hour before use. Coatings with several concentrations of TEOS were prepared. The formulations used are listed in Table 1. The one-pot coatings were prepared similarly with the exception that Milli-Q were added prior to HCl and that Octyltrichlorosilane (OTS, Thermo Scientific 97%) was added to the solutions after TEOS. The one-pot formulations are listed in Table 2.

Table 1: Mass ratios (wt%) for the different types of sols in the sol-gel formulations. HCl concentrations in parenthesis.

Formulation	TEOS	Fumed SiO ₂ 14 nm	HCl	Ethanol
0C	0	2.7	4.27 (1.0 M)	93.03
1A	5	2.5	2.63 (0.01 M)	89.87
1B	5	2.5	2.63 (0.1 M)	89.87
1C	5	2.5	2.63 (1.0 M)	89.87
2A	7.5	2.5	3.95 (0.01 M)	86.05
2B	7.5	2.5	3.95 (0.1 M)	86.05
2C	7.5	2.5	3.95 (1.0 M)	86.05
2D	7.5	2.5	3.95 (0.55 M)	86.05
3A	10	2.5	5.26 (0.01 M)	82.24

Table 2: Mass ratios (wt%) of the four different one-pot formulations.

Formulation	TEOS	Fumed SiO ₂	12M HCl	Milli-Q	OTS	Ethanol
O1	9.52	2.40	0.009	4.11	3.81	80.15
O52	5.10	2.45	0.009	4.19	1.91	86.34
O53	5.05	2.42	0.009	4.15	2.84	85.52
O54	5.00	2.40	0.009	4.11	3.75	84.72

3.1.3 Coating process

An illustration of the coating process is provided in Figure 7. OTS was added to the one-pot formulations after step 3. All samples were dip-coated (step 6) in the above formulations with submerging and withdrawal rates of 2 mm/s using a TA.XTplus texture analyser from Stable Micro Systems as a dipping robot. The samples were then post treated (step 7) either at 120 °C for 12 hours or calcined at 450°C for 4 hours with a ramp up of 1°C/min from room temperature and cooled down from 450°C by turning heating off. The hypothesis was that calcination would give more durable coatings by promoting the condensation reactions in the sol-gel process.

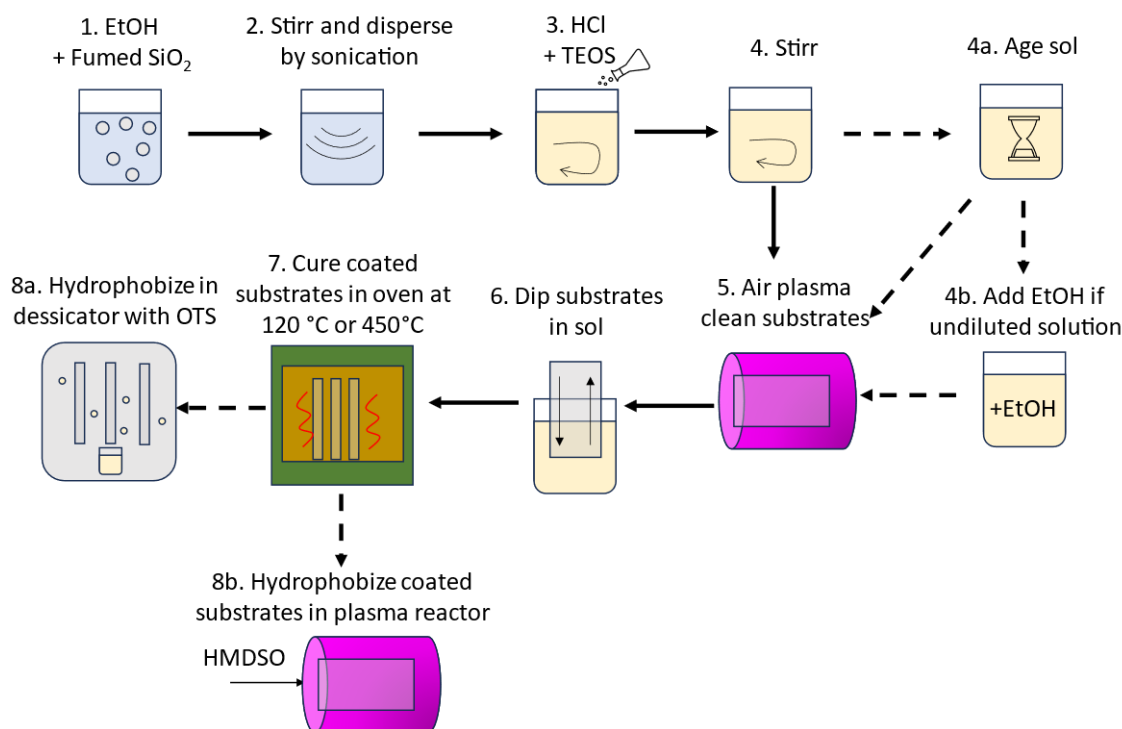


Figure 7: Flow chart illustrating the coating process. The standard SH silica coating protocol follows the solid arrows. Aged sols also include step 4a and 4b. The “one-pot” coating process ends at step 7.

Sets of samples to be hydrophobized were put in a desiccator with OTS and air was pumped out to 50 mbar and left for 24 hours to allow for self-assembly of a silane monolayer (step 8a). A second set of samples was hydrophobized by plasma polymerization of Hexamethyldisiloxane (HMDSO) (Fluka, 98.5% purity) in a plasma reactor (step 8b).

Some sols were dipped using sols that had been aged at room temperature for 4 days, corresponding to step 4a in Figure 7. Some samples were allowed to age for 1 day with a less diluted solution, only adding 3.3 % mass ratio of ethanol in step 1. Remaining ethanol was added at step 4b in Figure 7. The idea behind the latter approach was to promote the hydrolysis reaction of the sol-gel process (Eq. 12) to see if the film strength could be improved without loss in hydrophobicity and transparency.

The ready samples were named by sample type according to a system to easily identify substrate, formulation, posttreatment temperature, aging of the sol, how many times it was dipped and how it was hydrophobized. A full description of the sample type encoding is depicted in Appendix A.

3.1.4 Plasma polymerization

Plasma polymerization was used in two ways. The first was to apply a silica-like amorphous (SiO_x) barrier film on the glass substrates and the second was to functionalize the porous silica coatings to make them hydrophobic. The SiO_x film was primarily targeted at immobilizing Na^+ diffusing out from the glass substrates, especially at calcination, that could affect silanization. In order to do so, O_2 and HMDSO as precursors were led into a RF-plasma reactor at an O_2 to HMDSO ratio 10:1⁷⁰. The samples were mounted on a moving carousel in the reactor to allow for evenness, see Figure 8, and were processed at 100 W, for 1 or 2 minutes, to achieve film thicknesses of approximately 50 and 100 nm respectively⁷⁰. To hydrophobize the coatings by using plasma polymerization, a similar technique was used with the difference that no oxygen was supplied. As a result, the samples were covered by siloxane layers, forming a thin hydrophobic film on top of the porous silica coatings by non-polar methyl groups, as an alternative to hydrophobizing them in a desiccator with OTS, see 8b in Figure 7. Parameters for the plasma polymerizations are provided in Table 3.

Table 3: Parameters for plasma polymerization of glass and Si-wafers. HMDSO was used dip-coated samples to make them hydrophobic. SiO_x was used on bare glass as a passivation barrier prior to applying the porous silica coating.

Polymer	Precursors	Power [W]	Time [min]	Base pressure [mTorr]	Pressure with precursor [mTorr]
HMDSO	HMDSO	20	0.5	8	27
SiO_x	HMDSO + O_2	100	1	8.8	24.6
SiO_x	HMDSO + O_2	100	2	1.9	28.8

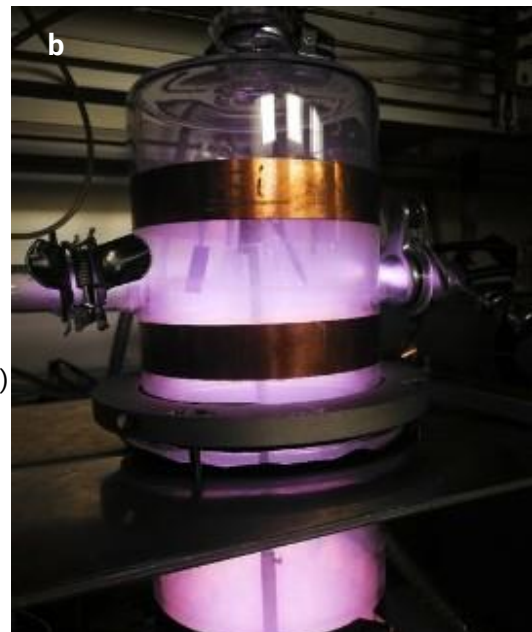
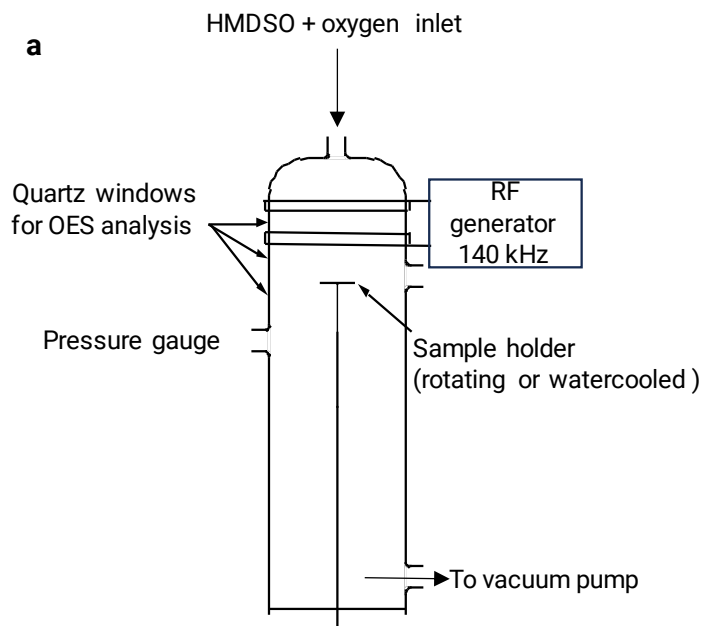


Figure 8: Plasma reactor at RISE facilities. (a) is a schematic view - gas enters the reactor continuously from the top while excess products are pumped out at the bottom. The sample holder in the middle rotates to allow for even application. A picture of the actual reactor while running in (b). The samples are oriented vertically and attached by clips.

3.2 Surface characterization methods

The developed coatings were characterized in terms of optical properties, wetting properties, thickness, ice-adhesion, and mechanical properties, including freeze-thaw cycles (FTC). A field test was conducted and evaluated for one of the coatings. The coatings were imaged by SEM and their surface chemical composition determined by XPS.

3.2.1 Optical transmittance

Since PV modules provide electricity by conversion from incoming photons, the amount and wavelength of light reaching the solar cells after hitting the cover glass is a key metric of the overall module performance. Sunlight hitting earth's atmosphere has a wavelength distribution approximating a blackbody radiator, but on its way through the atmosphere it is absorbed and scattered. To assess the optical transmittance for coated samples, their transmittance spectrums were recorded, and from that the solar weighted transmittance spectrum (T_{sw}) was calculated.

Glass slides were put in PerkinElmer Lambda 650 spectrophotometer perpendicular to the beam and transmittance spectrum for air-sample-air was recorded. The whole wavelength range of the instrument, 190-900 nm, was used. From the recorded spectrum, T_{sw} was calculated using the integral

$$T_{sw} = \frac{\int_{\lambda_a}^{\lambda_b} T(\lambda) I_{AM1.5}(\lambda) d\lambda}{\int_{\lambda_a}^{\lambda_b} I_{AM1.5}(\lambda) d\lambda} \quad (13)$$

where λ_a and λ_b gives the wavelength range, $T(\lambda)$ the transmittance measured, $I_{AM1.5}$ is a value coming from ASTM G-173-03 AM1.5 standard and corresponds to direct incidence solar light on a 39° tilted plane at ground level⁷¹. Eq. 13 was evaluated by using tabulated values of $I_{AM1.5}$.

3.2.2 Surface wettability

To study the wettability of the obtained surfaces, contact angle measurements were performed both at room temperature and below the dew point to characterize the hydrophobic properties. The measurements were done using a DataPhysics OCA40 micro instrument with a Peltier cold plate addition. Advancing and receding contact angle as well as roll-off angles were measured by tilting the table at a speed of 1.0 °/second for a 10 µL droplet. Calculation of CA was done with the software SCA20 using tangent leaning with fifth degree polynomial fitting, except for when evaluating samples below the dew point where ellipse fitting was used instead.

As the surface temperature drops, the wetting properties can change due to condensation of water vapour into the porous structure of the coating. If a Cassie-Baxter to Wenzel transition occur, not only will contact angle hysteresis drastically increase but also water will enter the surface microstructure and risk to damage it upon freezing. When SH surfaces are subjected to moist and at lower temperature, their CA tend to decrease while the CAH increases. This low temperature performance gives an indication on ice-repellency⁷². To evaluate the humidity tolerance of the samples, the substrate was put on a temperature controlled cold plate at 5°C and with room temperature at 23°C and 50% RH and letting it sit for 10 minutes, to let dew build-up before measuring static contact angle and roll-off angle.

3.2.3 Freeze-thaw cycling

As a stress and durability test for the coatings, a freeze-thaw cycling test was employed. An industry standard protocol IEC 62108⁷³ was used as a model. According to the standard, 24-hour cycles should be used, where each cycle constitutes 20 h at 85±2°C and 85±5% relative humidity (RH) followed by a 4 h period where temperature is lowered to -40°C for at least 30 min and then increased back to 85°C. However, in lack of a climate chamber (to reach the required % RH), another test procedure was used. That means the results can be used only to compare the relative performance of the coatings produced within the context of this project.

In this work, samples were put on a cold plate held at 5°C in a climate room with 50 % RH and held for 10 – 15 minutes until dew was accumulated on the surfaces. As the next step, samples were moved to a freezer held at -20°C for 60 – 90 min (except for overnight freezing occasions). Afterwards, the samples were then thawed in the climate-controlled room, see Figure 9. WCA including slide-off angle was measured after 4, 9 and 15 cycles. Without functionalization to make the porous silica coatings hydrophobic, they are very hydrophilic, so even minor damage will lead to pinning. In case the droplet did not slide off even at 90 degrees table tilt it was noted. As a measure of the resistance to pinning rate, freeze-thaw survival (FTS) was introduced. FTS was defined as

$$FTS = 1 - \frac{n_{pinned}}{n_{total}} \quad (14)$$

where n_{pinned} is the number of droplets pinned at 90 degrees tilt on sample for a test, and n_{total} is the total number of droplets measured on the same sample for that test.

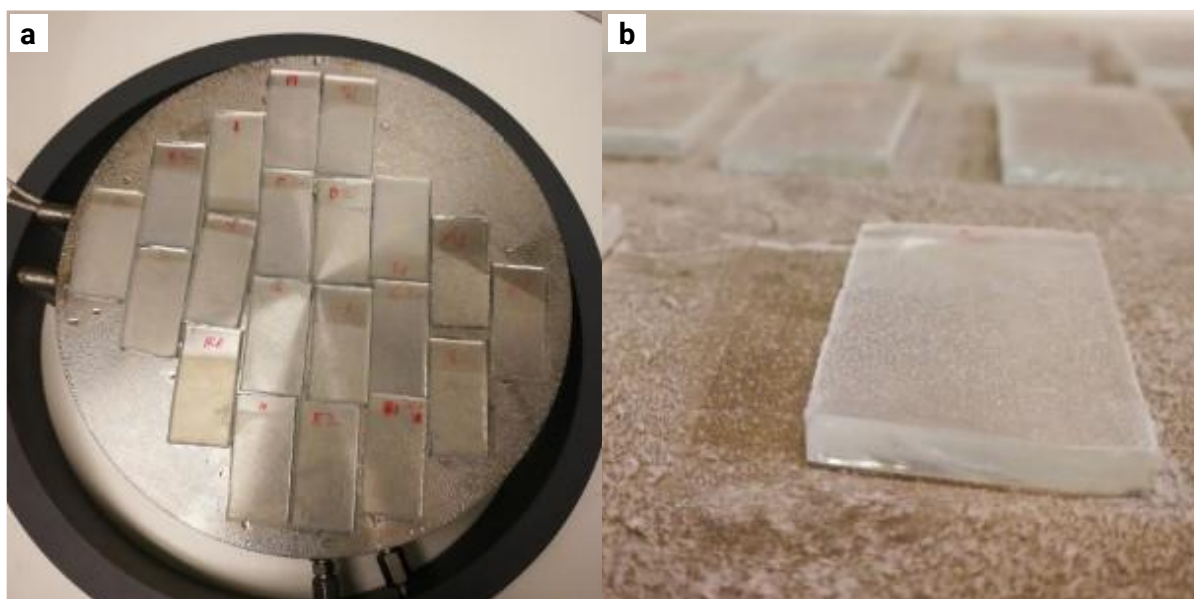


Figure 9: (a) Samples on a cold plate held at 5°C to allow for moisture to build up. The same setup was used for CA at dew point characterization as well as the freeze-thaw cycling. (b) Samples after freezing at -20°C.

3.2.4 SEM imaging

Imaging of the coatings was done to see how the structure varied between different formulations and to get a better understanding of how the coatings failed in tape peel testing (3.2.7). Scanning Electron Microscopy is a technique where a focused beam of electrons interacts with a solid surface. Backscattered or secondary electrons are recorded and by that an image is formed. The spatial resolution is on the order of single nm, but vacuum is needed, excluding some materials. Also charge build-up can be an issue for non-conducting samples. An Environmental SEM (ESEM) can work with higher pressures making it possible to image wet samples without dehydration⁷⁴. The SEM measurements was performed with a Quanta 250 FEG ESEM from FEI (Thermo Fisher Scientific).

3.2.5 Surface profilometry

Coating thickness and homogeneity are valuable information when developing coatings. For AR coatings, the thickness is a principal parameter. A surface profile can also be used to evaluate the coating method, for instance the effects of dipping speed and the formulation. A Bruker DektakXT Stylus profiler was used to determine coating thickness for selected samples. Stylus force was set to 1 mg, scan lengths 2, 3 and 4 mm, scan time was 60, 90 and 120 s, needle radius 2 μm , scan range 6.5 μm (vertical resolution 0.1 \AA), filters off. Scans were separated by approximately 1 mm. The samples were levelled with 2-point linear fit on bare substrate area.

3.2.6 Surface elemental analysis by X-ray Photoelectron Spectroscopy

X-ray Photoelectron Spectroscopy (XPS) was used to confirm the film composition and to look for presence and concentration of Na^+ from the glass substrates after being post-treated at 120 and 450, and weather the SiO_x barrier coating successfully prevented Na^+ diffusion. XPS, also known as Electron Spectroscopy for Chemical Analysis (ESCA), is a highly surface sensitive and powerful tool for surface chemical analysis. The XPS method provides the surface chemical composition for the outermost 2-10 nanometres of surfaces. The analysis depth depends on the material analysed and is less than 10 nm for metal oxides and metals. XPS provides quantitative data on both the elemental composition and different chemical states of an element (different functional groups, chemical bonding, oxidation state, etc.). All elements, except hydrogen and helium, can be detected, and the surface chemical composition obtained can be expressed in at%. It is straightforward to quantify the XPS data, since there is no need to run any reference samples. The instrument used was a Kratos AXIS Ultra^{DLD} with a monochromatic Al X-ray source and the analysis area was smaller than 1 mm^2 , with most of the signal from an area of about 700 x 300 micrometres.

3.2.7 Tape peel testing

Tape peel testing has previously been used by Zhao et al.⁷⁵ to evaluate the strength of silica based superhydrophobic coatings. The working principle is that a piece of tape is rolled on the surface to be tested and then peeled off with a device attached to a force sensor. Both roll-on and peeling are done automatically in a controlled fashion to allow for consistent results. Given there is no adhesive failure between the tape and the surface, the peel force will give an indication on the strength of the coating, or its adhesion to the underlying substrate. In this project slip and peel tester Imass SP-2000 and 3M Scotch Crystal 19 mm tape following the standard testing procedure ASTM D3330 was used. Figure 10 shows a schematic drawing of the setup. Roll-on was done with 5 mm/s and the specified roller weight of 2040 g back and forth two times to attach the tape to the sample. The tape was then peeled off at a 180-degree angle at a speed of 2.5 mm/s. The peel force was sampled using a computer and the software Comlink 3.0. The peel force data was exported and analysed. To get accurate averages of the peel force it was necessary to manually select areas of interest, see Figure 11.

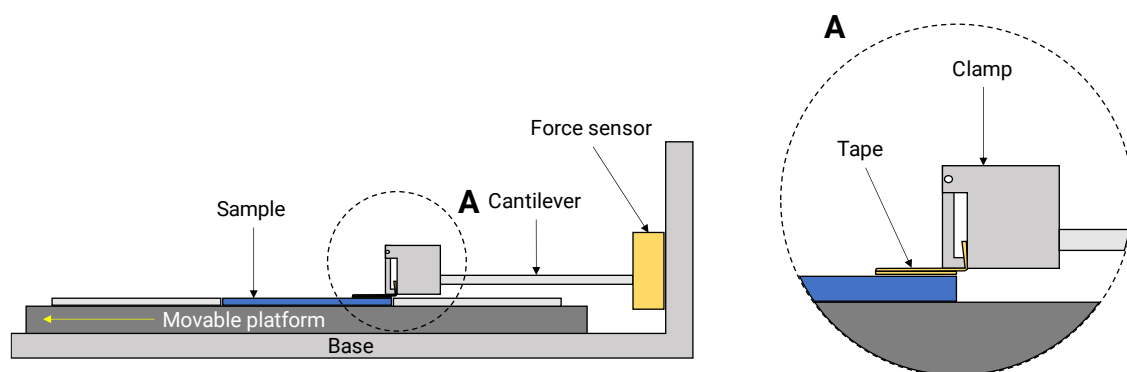


Figure 10: Slip and peel tester used for tape peel tests. One end of the tape is attached to the clamp. The peeling happens when the motorized platform moves to the left in the picture. Force is sampled by the force sensor. “A” marks a section of the clamp.

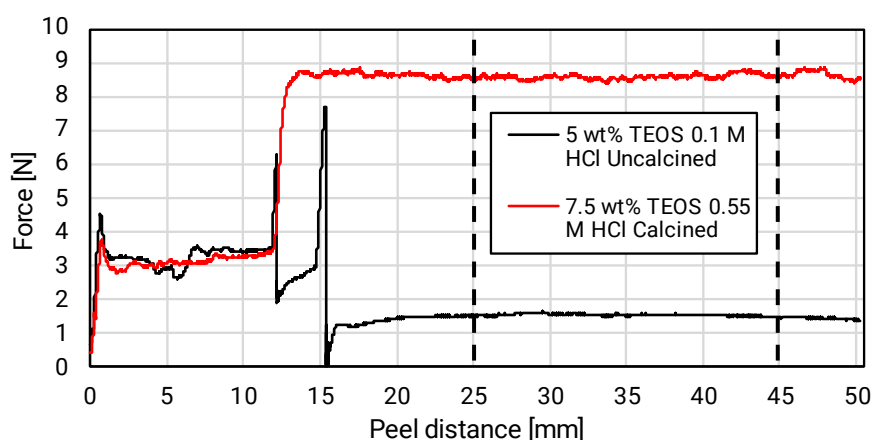


Figure 11: Example of force versus distance plot for SH coatings with different formulations and post-treatment temperatures. Edge effects and lower values on the left part of the graph from peeling tape from outside the sample. The values around 3 N reflect the tape adhesion to uncoated glass. Vertical dashed lines indicate the averaging interval.

3.2.8 Ice adhesion

As for the tape peel test, the Imass SP-2000 slip and peel tester was used, with a cold plate add-on (Model SPA2-05). Samples were cooled on cold plate below dewpoint (5°C at 23°C 50% RH ambient conditions) for 10 minutes. A cuvette was placed on top of each sample and held in place with an inverted lab jack, see Figure 12a, filled with 1 ml of deionized water (Milli-Q type 1 water) and put in a freezer at -10°C for 2 hours. After freezing, the sample was moved to a Peltier cold plate attached to the movable platform on the slip and peel tester where the maximum force was recorded, see Figure 12b for an illustration. The ice adhesion (a shear stress) was calculated by dividing the force by the ice-sample interface area (1 cm²). The ice adhesion testing was repeated 3 times on the same spot to evaluate the coating durability. To compare the results with glass reference, the adhesion reduction factor (ARF) was calculated as the ice adhesion of glass divided by the ice adhesion of the coated samples.

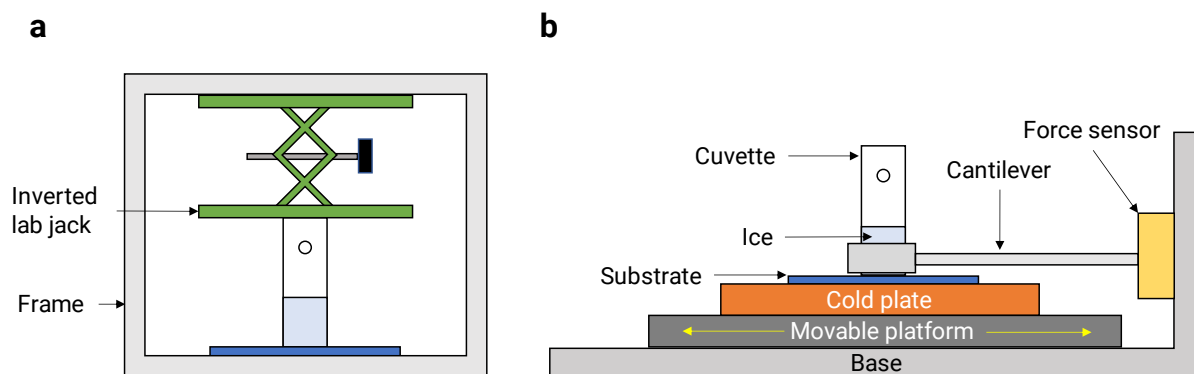


Figure 12: Ice adhesion setup. (a) illustrates how samples were prepared and frozen prior to testing. In (b) the same slip and peel tester used for tape peel tests was employed. A Peltier element cold plate was attached to the movable platform. The samples with the ice were held in place on the cold plate.

3.2.9 Field test for snow and ice shedding evaluation

Since lab test have limitations, for instance snow is very difficult to replicate, a field test was done on a superhydrophobic sample of type GL510CO (5 wt% TEOS, 0.01 M HCl, calcined and hydrophobized by OTS). It was, together with other samples including a glass reference, mounted on a balcony in Stockholm Hägersten, on January 13th, 2023. Photographs were taken and temperatures recorded after notable precipitation events until the field test was aborted on March 28th, 2023. The samples were mounted 25 cm apart, on the balcony railing and approximately parallel to the ground, making sliding of ice and snow more difficult than with a tilt.

4. Results and Discussion

4.1 Chemical analysis

For calcined coatings, hydrophobization (HP) by OTS was sometimes unsuccessful, often with pinning of droplets. Since hydrophobizing calcined coatings on silicon wafers using the same method did not pose any issues and hydrophobizing coated glass samples post-treated at 120°C was consistently successful, sodium ions present on the surface was likely the reason for the pinning of droplets. Primarily to look for presence of Na⁺, XPS analysis was therefore performed on both uncoated glass and coated glass that had been heated to 120°C and 450°C. Coated Si-wafers were analysed as references, to make sure there was no other origin of sodium than the substrates, such as the coating themselves or the ovens used. As expected, coatings on glass substrates calcined at 450°C had significant amounts of sodium present (0.55 at%) compared to not calcinated samples (0.02 at% Na), see Table 4. For coatings on silicon wafers, no sodium was detected regardless of post-treatment temperature, proving the source of the sodium was diffusion from glass substrates. Detailed XPS results are provided in Appendix C, Table II – Table VII.

Table 4: Amount of Na⁺ in at% as determined by XPS analysis.

	120°C	450°C
Coated Si-wafer	-	-
Coated glass	0.02±0.01	0.55±0.02
Uncoated glass	5.12±0.36	7.14±1.14

4.2 Optical transmittance and coating thickness

All coatings produced were transparent. To illustrate the general characteristics of the optical behaviour of the coatings, UV-vis transmittance spectra from spectrophotometer measurements for a selection of samples are shown in Figure 13. Most coatings exhibited peak transmittance values at around 500 and 900 nm, hinting at similar density and thickness (Section 2.2). The peaks reach up to 95%. However, especially at wavelengths below 500 nm, all but a few samples showed lower transmittance than uncoated glass. From the UV-vis spectroscopy scans the solar weighted transmittance (TSW) was calculated using Eq. 13 (All TSW values are provided in Table I).

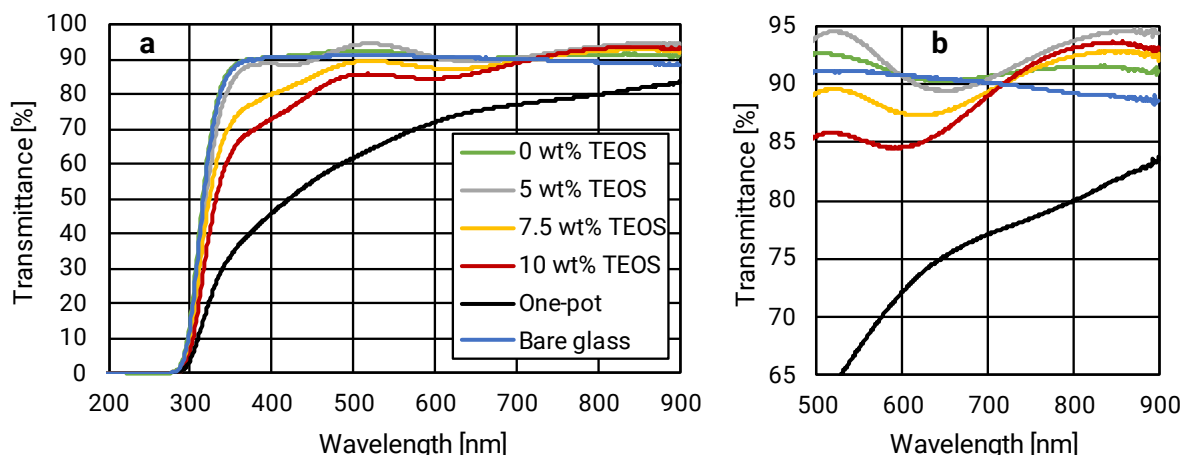


Figure 13: Plot showing transmittance spectra of selected samples. (a) shows the full measured spectrum while (b) is a section for better visibility. Bare glass is included for reference.

The coatings measured a TSW of 87% on average, a very good result for superhydrophobic coatings. Coatings with 0 and 5 wt% TEOS were roughly equal to uncoated glass whereas coatings with 7.5 and 10 wt% TEOS had slightly lower TSW on average. The one pot-coating (amounting to 9.5 wt% TEOS) performed notable worse than glass reference, suggesting the incorporated OTS have a significant effect

on the coating structure. Coating thickness was measured with profilometry on two samples, both dipped twice but with different amounts of TEOS, listed in Table 5. GL710CO has a TSW of 0.89 and GL110CO has a TSW of 0.85, confirming that coating thickness isn't proportionally related to optical transmittance. The profilometry plots are found in Appendix B, Figure B.I and Figure B.II.

Table 5: Profilometry results for coated glass.

SAMPLE TYPE	FORMULATION	TEOS [wt%]	THICKNESS [nm]
GL710CO	2A	7.5	545±49
GL110CO	3A	10	514±35

Three distinct coating structures could be distinguished from the SEM images. Figure 14 shows pictures and SEM micrographs from samples with 0 wt% TEOS, 10 wt% TEOS and a One-pot samples with 9.5 wt% TEOS. Without TEOS, the coating is hardly visible by eye as in Figure 14(a). On the microscale, Figure 14(b)-(c), the surface appears anisotropic with elongated pores while on the nanoscale, Figure 14(d) it has a hierarchical structure. Samples with 10 wt% has a clearly visible coating, see Figure 14(e) where the upper edge of the sample that has not been dipped is contrasted. The SEM images in Figure 14(f)-(h) reveal that the structure is denser and more isotropic than for the coating without TEOS. Comparing Figure 14(d) with Figure 14(h) reveals that TEOS leads to agglomeration of particles and a courser nanostructure. The increased density from the TEOS result in a lower transmittance. The one-pot samples that had transmittance curves with different characteristics than the other samples without peaks for the wavelength range measured (Figure 13) also showed an unexpected structure in the SEM images with spots in distinct size range of 2 μm and 4 μm , see Figure 14(j)-(k). At further magnification Figure 14(l), the structure is similar as that for 10 wt% TEOS but overlaying the spots.

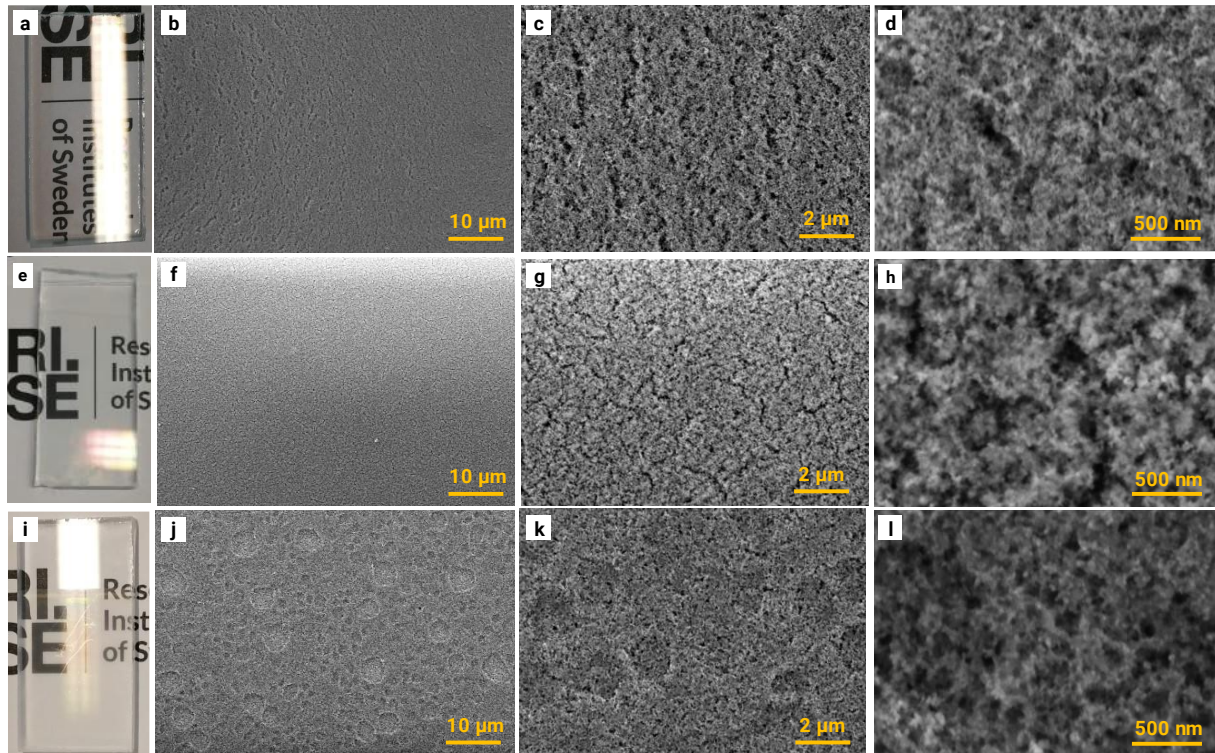


Figure 14: Photographs and SEM images of SH samples. (a)-(d) from samples with 0 wt% TEOS, (e)-(h) samples with 10 wt% TEOS and (i)-(l) One-pot samples with 9.5 wt% TEOS.

Figure 15(a) shows the solar weighted transmittance against TEOS concentration for all measured coatings. Uncoated glass has a TSW of 0.90, so samples with 0, 5 and 7.5 wt% TEOS were made with higher transmittance than the reference. It is a clear trend however, that increasing TEOS content from

5 wt% decreases transmittance. The highest TSW was 91.5% for coatings with both 5 wt% and 7.5 wt% TEOS.

There is a less strong correlation between optical transmittance and variation in HCl concentration, as seen in Figure 15(b). However, the transmittance does slightly decrease as HCl concentration increases.

Aging of the sols affects the transmittance, as seen in Figure 15(c). The non-aged sols with 5 wt% TEOS measured higher transmittance than the sols aged 4 days, while for 7.5 wt% TEOS, the opposite seems true, but that may be due to an outlier shifting the average value. For the undiluted sols, however, aging had a negative effect on transmittance regardless of formulation.

Calcination is slightly beneficial for optical transmittance for samples with 5 wt% TEOS as shown in Figure 15(d). This may be due to that the elevated temperature removes unreacted species, altering average density and/or light absorption.

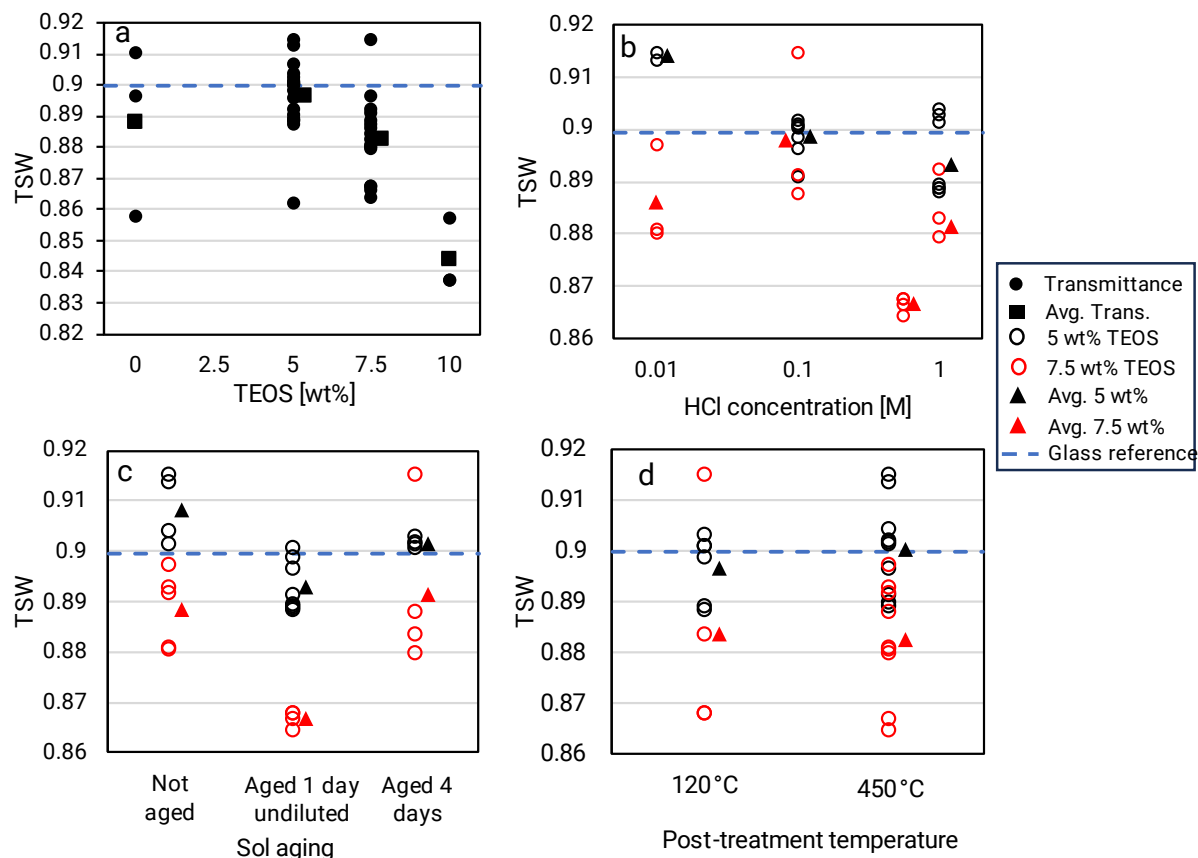


Figure 15: Plots of the solar weighted transmission (TSW). (a) shows TSW by TEOS concentration for all measured samples except One-pot. (b) shows TSW vs HCl concentration. (c) Shows TSW plotted for the different aging protocols. (d) shows TSW plotted for by the different post-treatment temperatures used.

4.3 Wetting

All coatings achieved strong hydrophobicity with WCA ranging from 135°-160°, to be compared with cleaned (IPA followed by rinsing with ethanol, water and dried with compressed air) bare glass that measured 11°. Roll-off angle measured between 2° and 24° compared with glass that had an average slide-off angle of 20° and a CAH of 13°. Figure 16 shows droplets on both glass and a superhydrophobic coating on glass. It is important to note for glass though, that after sliding off, there was residual water left on the samples. The most hydrophobic coatings on glass substrates were the ones hydrophobized with OTS. OTS on coated substrates with SiO_x barrier had less hydrophobic properties. What influence the SiO_x protective layer has on the coating and why remains unknown. Hydrophobization by HMDSO proved less effective than by OTS. That might be due to thicker silane layers, partially filling voids in the porous coatings. The one-pot coatings did not achieve superhydrophobicity, but the formulation O1 with higher TEOS concentration (9.5 wt%) was more hydrophobic than formulations (O52, O53 and O54) with lower TEOS amount (5 wt%). Either the structure (Figure 14) or too low amounts of OTS could be the reasons for this.

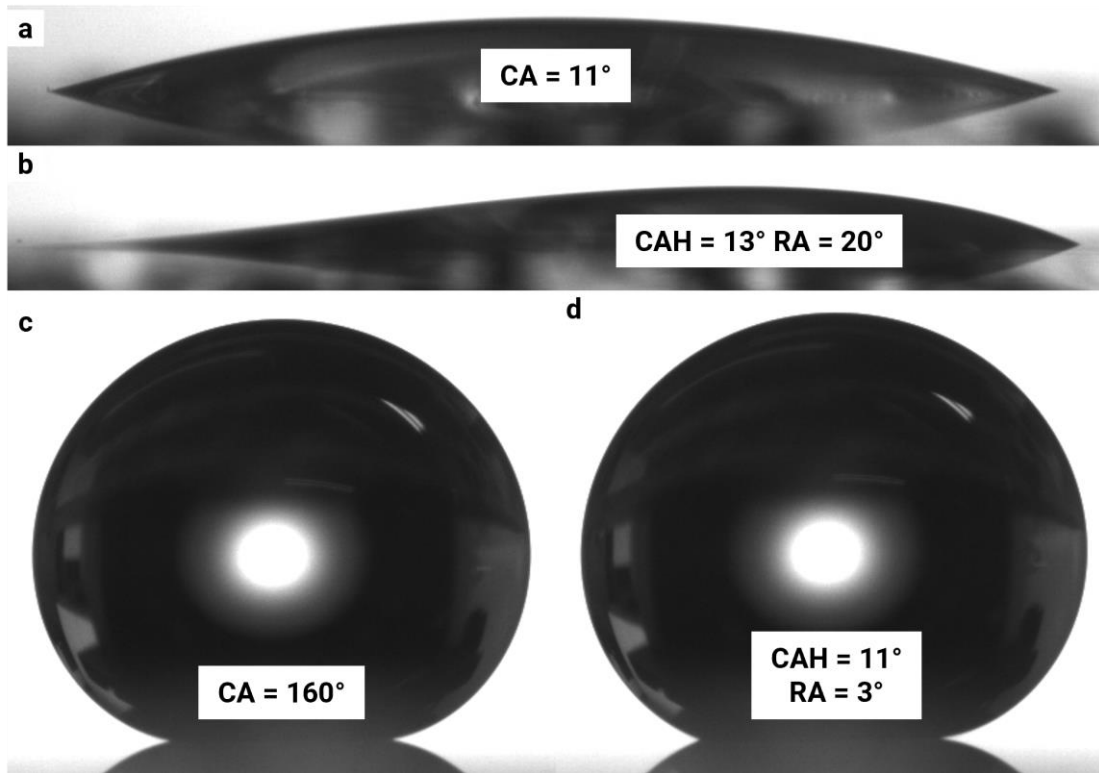


Figure 16: Droplets on uncoated cleaned glass (a)-(b) and glass with superhydrophobic coating GL510CO (5 wt% TEOS and OTS) (c)-(d). (a) and (c) show static droplets with CA as the average between right and left contact angle. (b) and (d) are snapshots of droplets just prior to the droplets sliding (to the right in picture). CAH is the difference between advancing (right) and receding (left) contact angle. RA is the roll-off angle.

Figure 17 shows contact angles and roll-off angles plotted against TEOS concentration. Results for superhydrophobic silica coatings with OTS on glass are shown with black circles. These coatings on average have the highest WCA and the lowest RA, compared to coatings on SiO_x , shown with red circles and coatings hydrophobized using HMDSO in blue squares. Higher TEOS concentration also clearly positively affects hydrophobicity for OTS-hydrophobized coatings on glass.

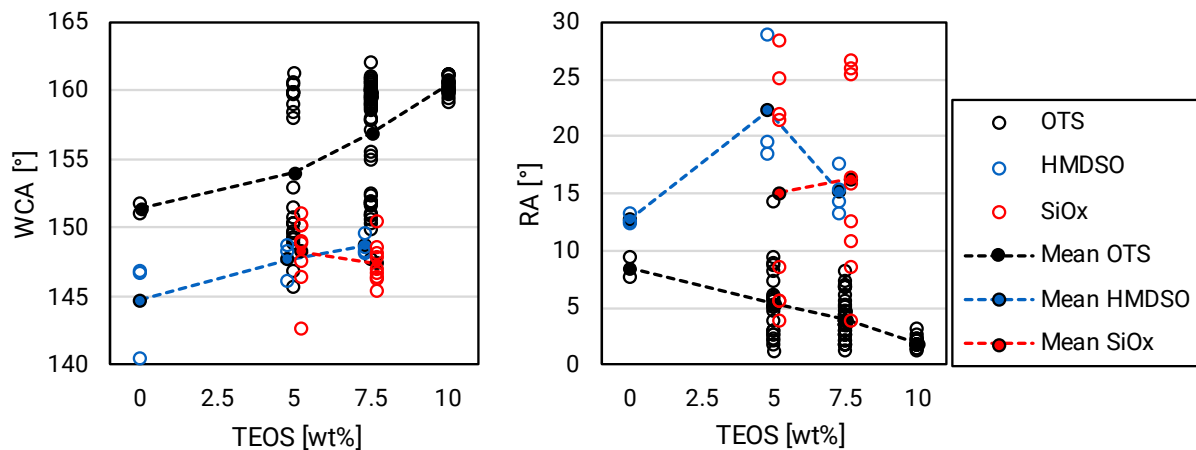


Figure 17: Static water contact angles and roll-off angles by TEOS concentrations. OTS denotes samples hydrophobized by OTS on glass substrates, SiO_x are similar coatings but on SiO_x coated glass substrates. HMDSO denotes coatings on glass hydrophobized by HMDSO. Dashed lines between the mean values are for readability.

By instead varying for HCl concentrations, as shown in Figure 18, it seems that less HCl has a positive impact on hydrophobicity. The pattern that more concentrated HCl gives less hydrophobic surfaces still holds when isolating SH surfaces fabricated by OTS on coatings dipped on glass.

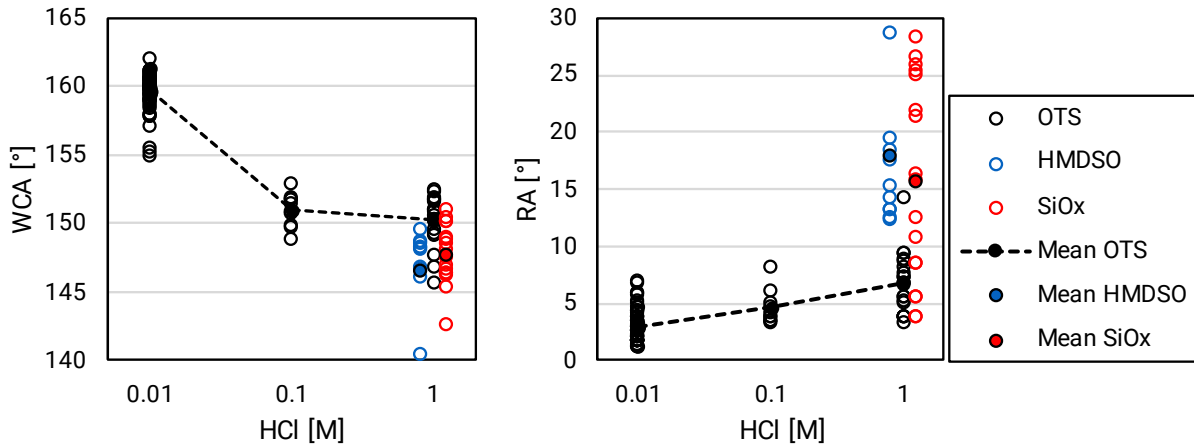


Figure 18: Static WCA and roll-off angles by HCl concentrations. OTS denotes samples hydrophobized by OTS on glass substrates, SiO_x are similar coatings but on SiO_x coated glass substrates. HMDSO denotes coatings on glass hydrophobized by HMDSO. The dashed line between the mean values is for readability. HMDSO and SiO_x type coatings were only produced with 1 M HCl concentration.

In general, calcination at 450°C affected hydrophobicity positively for coatings on glass hydrophobized by OTS, as evident from Figure 19. That is despite the sodium ions coming from the glass. One reason for that was due to a systematic error, only including successfully hydrophobized samples in the test suite. Nonetheless it is an important result, since if the silane successfully binds to the calcined coatings, they will become more hydrophobic than those coatings post-treated at 120°C.

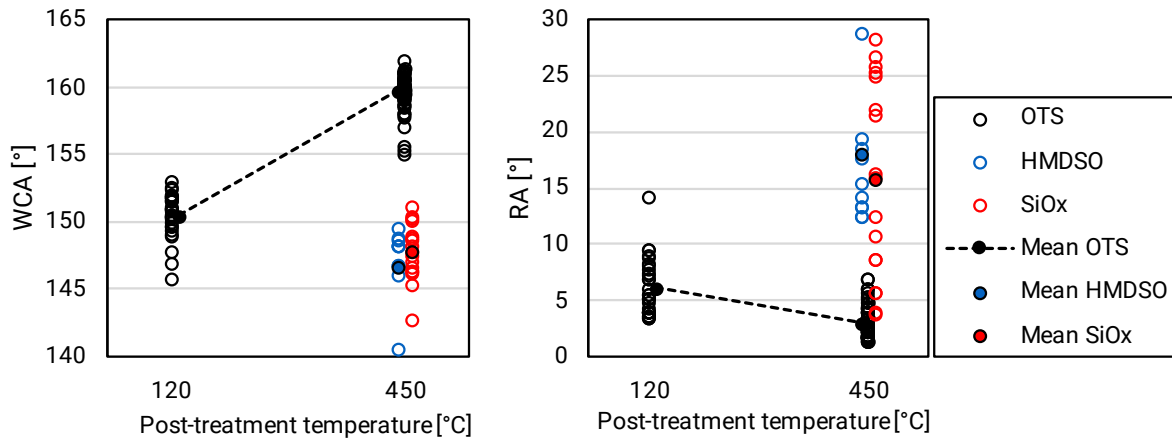


Figure 19: Static WCA and roll-off angles by post-treatment temperature. OTS denotes samples hydrophobized by OTS on glass substrates, SiO_x are similar coatings but on SiO_x coated glass substrates. HMDSO denotes coatings on glass hydrophobized by HMDSO. The dashed line between the mean values is for readability. HMDSO and SiO_x type coatings were all calcined at 450°C.

Figure 20 shows the correlation between room temperature and dewpoint roll-off angle. The aim with the dewpoint test was to see if some coatings stood out in this regard i.e., show better humidity tolerance, and whether that could be connected to other cold condition tests as well as durability. The dewpoint RA follows the RA at room temperature with a correlation $r = 0.87$. Samples with relatively low dewpoint roll-off angle (RADP) are those hydrophobized with HMDSO (GL030CH, GL530CH and GL730CH) and 7.5 wt% TEOS with OTS (GL730BO). One-pot (GL130B1) and 0 wt% TEOS with OTS had relatively high RADP.

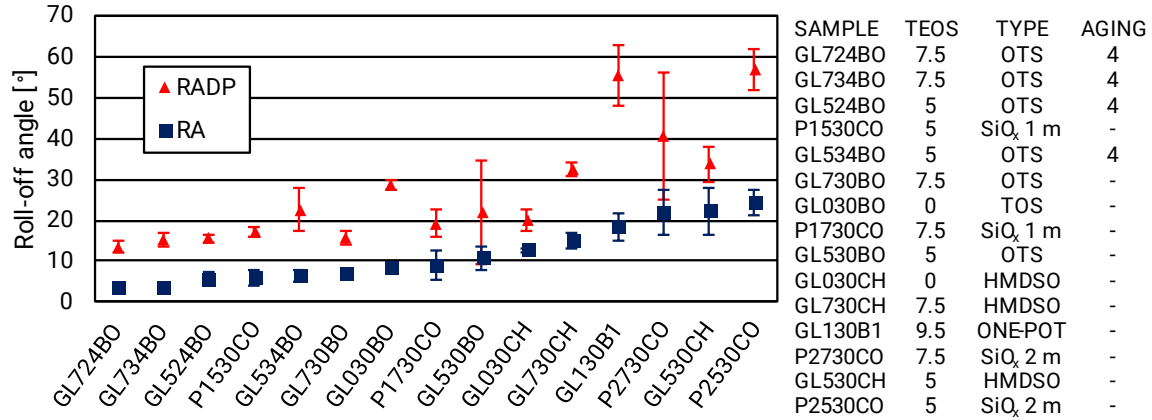


Figure 20: Roll-off angles (RA) at room temperature and at dewpoint (RADP) by sample type in order of ascending RA to illustrate how RA and RADP are linked. Full description of the sample types is listed in Appendix C, Table X.

The strongest performers overall in the dewpoint test (that is, with the lowest values) were samples dipped with sols aged 4 days and hydrophobized with OTS, and among those was 7.5 wt% TEOS better than 5 wt% TEOS. After those, the samples with coatings on 1 min SiO_x performed the best. Samples that are less likely to enter a fully wetted Wenzel state when subjected to humid conditions will be more humid resistant. The difference between coating types is likely due to variations in morphology, where the more humid resistant coatings have a more hierarchical surface structure. There is a general tendency that the roll-off angle is negatively correlated to WCA and coatings with WCA $\geq 160^\circ$ all have single digit roll-off angles. The plot in Figure 21 illustrates this relation between static contact angle and roll-off angle. The CA results for all samples are ordered by ascending roll-off angle from left to right, while static contact angle generally is descending. Notable exceptions are GL724BO, GL734BO, GL524BO and GL534BO; all sols that were aged 4 days prior to dipping. Despite relatively low static CA they had remarkably low roll-off angle, pointing at low CAH. The other exceptions are the coatings on SiO_x film, that is P1530CO, P1730CO, P2530CO and O2730CO. For both cases, the reason for the low roll-off may be due to higher smoothness or less coating defects but it can also be attributed to a different surface structure.

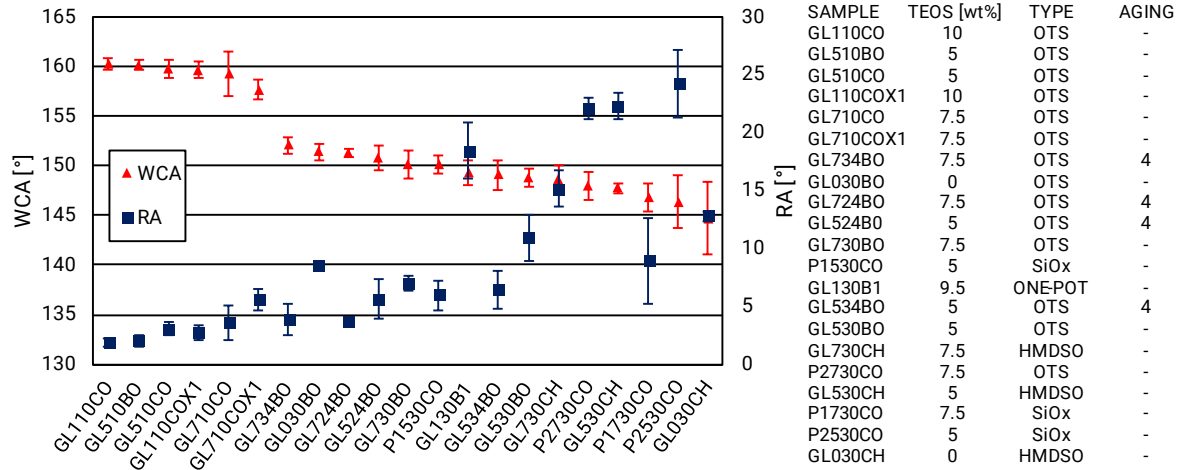


Figure 21: Average water contact angles and roll-off angles in order of descending contact angle. The sample types are listed in Appendix C, Table X.

4.4 Tape peel results

The peel tests showed stark contrast between different coatings where the strongest outperformed the weakest more than five times. Higher amount of TEOS in the sols increased the coating strength, as can be seen in Figure 22(a). When instead looking at the variation of the acid concentration, Figure 22(b), there is tendency towards stronger coatings as HCl molarity is increased for 5 wt% TEOS. However, the importance of HCl concentration is not as strong as the TEOS concentration regarding the coating strength. Aging of the sols prior to dipping gave mixed results as seen in Figure 22(c), with the highest

strength achieved for coatings made of sols aged undiluted. Finally, the post treatment temperature had a clear effect on the coating strength, especially for sols with 7.5 wt% TEOS, see Figure 22(d).

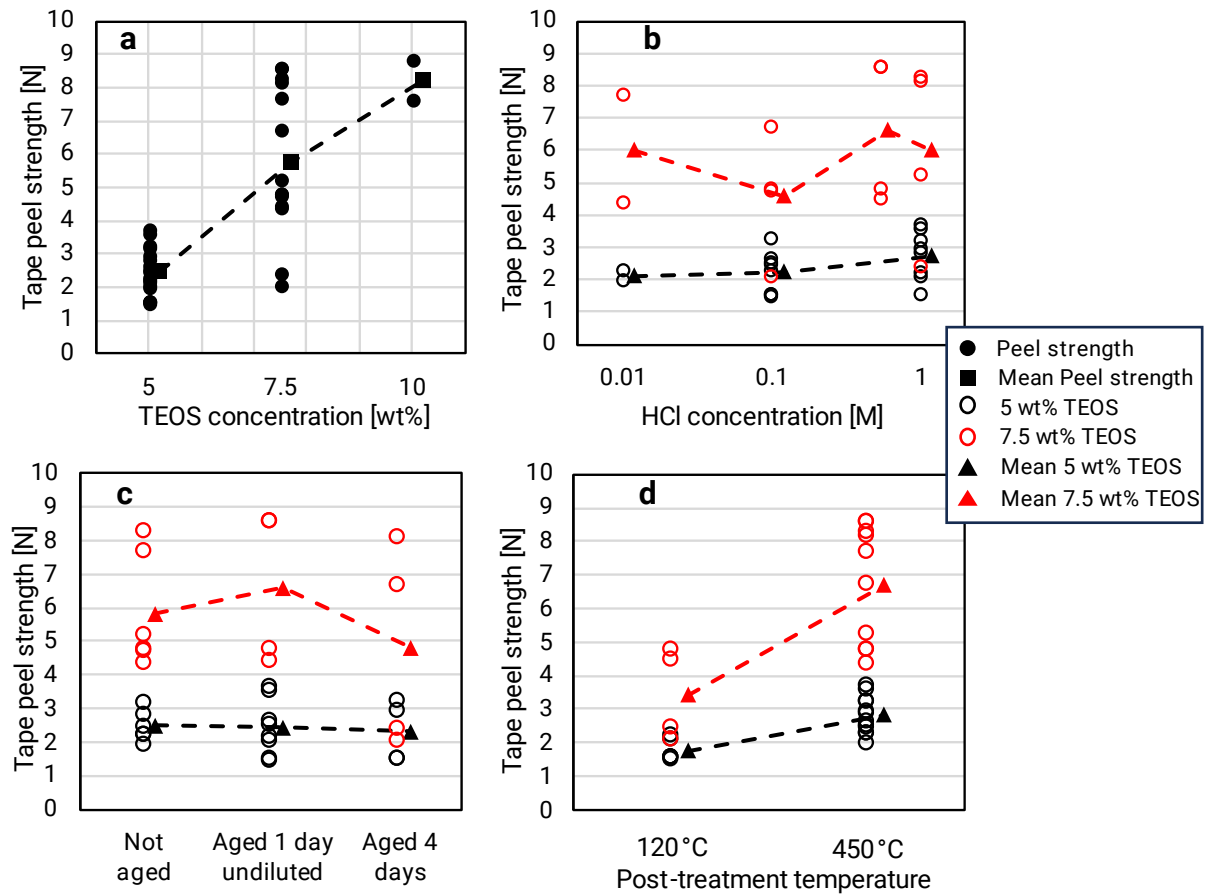


Figure 22: Coating strength as evaluated by tape peel test. (a) Shows peel strength by TEOS concentration for all samples as circles. (b) Shows peel strength by HCl concentration. (c) Shows peel strength by aging and (d) shows peel strength by posttreatment temperature. The dotted lines provide guidance for the eye.

Figure 23 shows SEM micrographs and photographs of two of the peeled samples. One of the strongest coatings, GL734C with 7.5 wt% TEOS, 1 M HCl, aged 4 days prior to dipping and calcined at 450°C is pictured in Figure 23(a)-(c) and one of the weakest coatings tested, GL534B that had 5.0 wt% TEOS, 1 M HCl, was aged 4 days prior to dipping and not calcined is pictured in Figure 23(d)-(f). In Figure 23(a), residue of the tape that have failed cohesively can be seen, pointing at the coating, at least in some areas, are stronger than the tape. In Figure 23(b) the glass substrate is visible, pointing at substrate adhesion being the point of failure in some areas. From Figure 23(c) it is clear where the tape was attached. In Figure 23(d), the peeled area is formed into parallel grooves, about 100 μm apart, likely caused by the stick-slip effect that sometimes occurs during adhesive tape peeling^{76,77}. In Figure 23(e), islands of remaining coating material are visible and patches of the naked glass can be seen and in Figure 23(f), the photograph post peeling shows that it is difficult to visibly recognize that the sample has been peel tested, contrary to the sample with tape residue in Figure 23(c). Only on the left edge, where the transition zone is between bare and coated glass, damage is visible. That would correspond to the plot in Figure 11, where there is a force peak in the transition zone. In summary, the strongest coating showed a mixture of adhesive failure between the coating and the substrate and failure within the tape, whereas the weaker coatings exhibited both cohesive and adhesive failure. That points towards improved adhesion could have improved peel strength even more for the best coatings, but likely had not improved coating durability when it comes to the intended use case on cover glasses for solar cells, since the strength of the top side of the coating and the hydrophobicity are the most important properties in that regard.

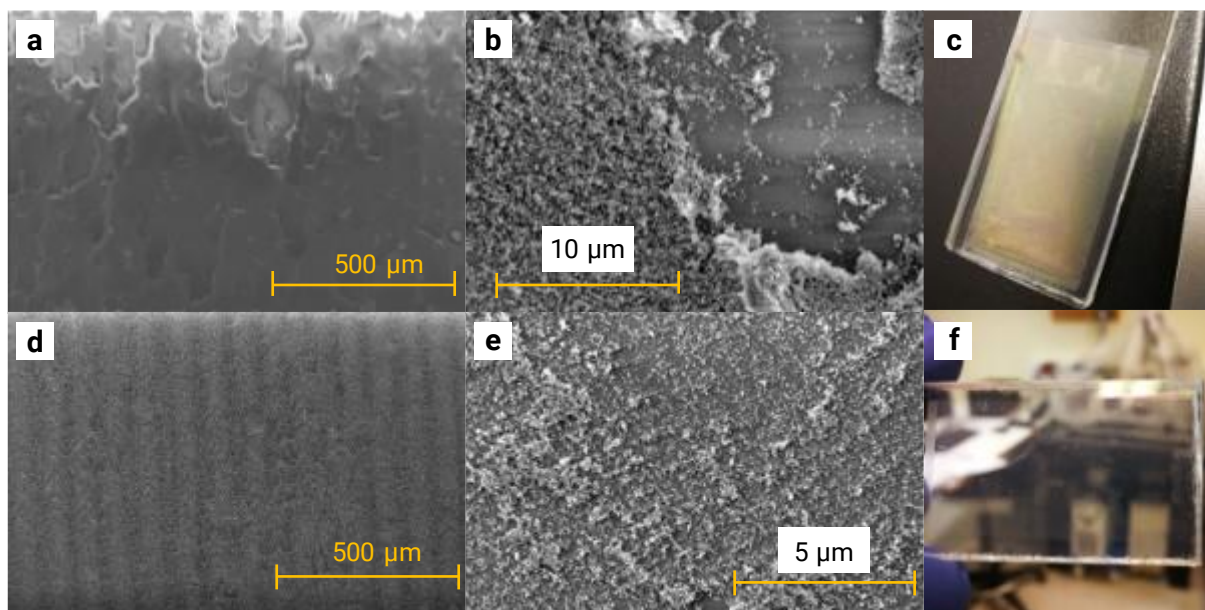


Figure 23: Pictures of tape peeled samples. (a)-(c) are of a calcined sample with 7.5 wt% TEOS (GL734C) and a high peel strength of 8.14 N. (d)-(f) are of an uncalcined sample with 5 wt% TEOS (GL524B) and significantly lower peel strength of 1.51 N. (a) shows a lamellar structure and in (b) parts of the glass substrate is visible. (d) show that the tear formed valleys (e) the glass substrate is not exposed. A photograph of the same sample in (f).

4.5 Freezing resilience

20 samples were subjected to the freeze-thaw cycle stress test. The sample selection was based on systematically testing a diverse range of hydrophobic coatings to see what patterns would emerge. Substrates were glass and glass with SiO_x barrier coatings of two different thicknesses. There are 4 TEOS weight ratios, 0, 5, 7.5 and 10 wt%. (The one-pot samples have a 9.5 wt% TEOS-ratio). Two different catalyst concentrations (excluding the one-pot formulations), two post-treatment protocols (120°C and 450°C). Finally, there are 3 types of hydrophobization methods: OTS self-assembly in desiccator, plasma polymerization by using HMDSO as precursor and one-pot that has OTS included in the sols. Table X in Appendix C holds the complete sample matrix including test labels and results.

The water contact angle, as well as roll-off angle was measured after 4, 9 and 15 freeze-thaw cycles. Most coatings had experienced damage, often visible to the naked eye, leading to droplets not sliding off the surface when tilted, because of pinning. From Figure 24(a), it is clear that damage has happened while Figure 24(b)-(d) all look homogenous. However, sample M in Figure 24(d) did degrade substantially during the freeze-thaw stress test, hinting at possibly different failure mechanisms.

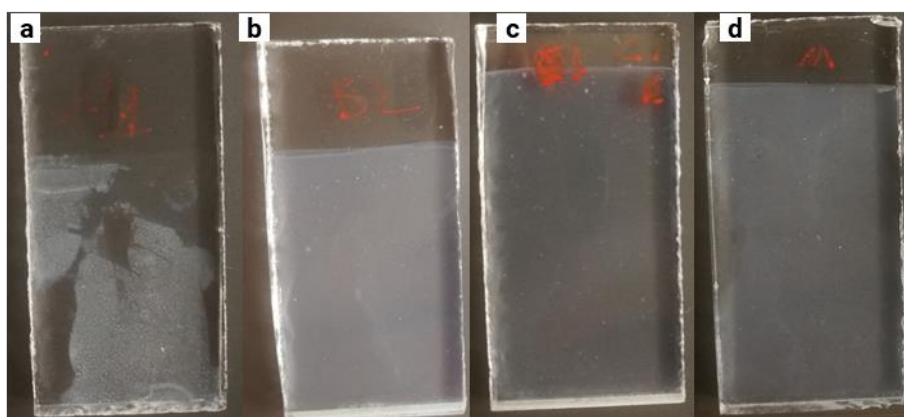


Figure 24: Photographs of samples after 15 freeze-thaw cycles. (a) sample A1, 0 wt% TEOS, OTS. (b) sample B2, 5 wt% TEOS HMDSO. (c) sample C1, 7.5 wt% TEOS, HMDSO. (d) sample M, 10 wt% TEOS, OTS.

After 15 cycles, 2 samples out of the 20 tested achieved a 100% survival (see Table 6). Those, labelled B2 and C1 were both hydrophobized by HMDSO in the plasma reactor, although with different TEOS content, 5 wt% and 7.5 wt%. While these samples were not the most hydrophobic initially, they performed

best in the freeze-thaw cycling, perhaps because the HMDSO-coatings are thicker than or better crosslinked than the OTS-layers, which then improve durability. While all applied droplets did slide off, the roll-off angle increased from 13° to 30° for sample B2. For C1, no increase in RA could be observed even after 15 freeze-thaw cycles. However, for both, the static CA surprisingly slightly increased after 15 cycles. Sample C1 had virtual zero loss of transmission after the freezing test, while there was a transmission drop for B1 amounting to about 3 percentage point TSW, also evident from Figure 24(b), where the coating appears milky.

Table 6: CA measurements for the only samples with 100% survival in freeze-thaw stress test, and TSW before and after the freeze-thaw cycling test.

SAMPLE TYPE	LABEL	TEOS [wt%]	WCA [°]	RA [°]	RADP [°]	15 FTC WCA [°]	15 FTC RA [°]	TSW [%]	15 FTC TSW [%]
GL530CH	B2	5	145±4	13±1	20±3	151±3	30±8	86.2	83.0
GL730CH	C1	7.5	148±1	22±6	34±5	154±3	20±3	88.5	88.2

Surviving roll-off values for all samples after 15 cycles are found in Table X in Appendix C, and are presented as averages. There were notable differences between the HMDSO samples, however. The reason may be linked to their positioning in the plasma reactor. Although the samples were attached to a carousel for even coating, they were placed at different radii, and not angled perfectly. That can be seen in Figure 8(b). Coatings dipped once have shown to be less consistent with regards to wetting, likely due to areas with less coverage. Here, for coatings with 7.5 wt% TEOS, it was evident that sample L, dipped once, was less resilient than sample F1 and F2, dipped twice, despite the former being calcined, increasing its strength substantially. It was expected to see a correlation between coating strength measured by peel force and freeze-thaw durability, hence higher TEOS concentration as well as higher post-treatment temperature should prove more durable. It may also be that the thickness and strength of the hydrophobization layers plays a role since freezing water will damage any of the porous silica coatings. Figure 25(a) shows how average contact angles vary with freeze-thaw cycles for sample A1 that performed worst in this regard, B2 and C2 that performed best and sample I that was an average performer. Figure 25(b) shows the same samples but plotting survival instead of WCA.

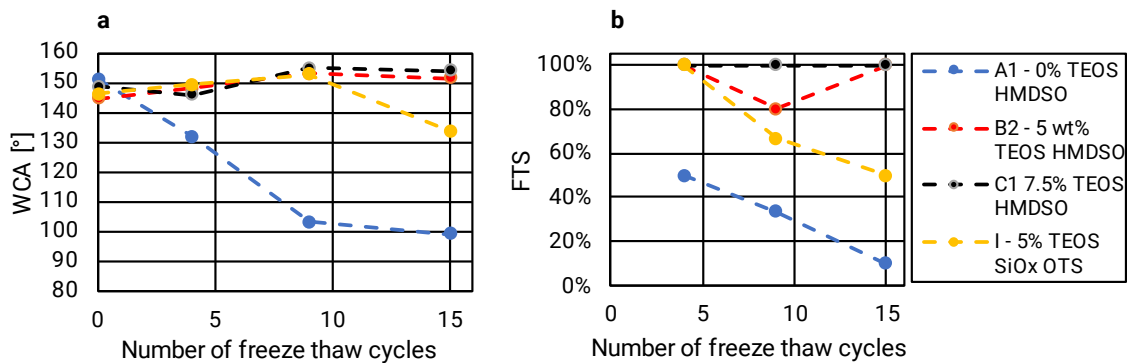


Figure 25: Average WCA and freeze-thaw-survival (FTS) by number of freeze-thaw cycles. The lines are there to guide the eye.

Another observation to point out is that some increment of the static contact angle could be seen during the test, visible in Figure 25(a). All CA tests were done in a climate-controlled room, ruling out humidity and temperature variations as the cause. Calcined samples should be chemically stable over time. One hypothesis is that moisture was being trapped within the structure during the freeze-thaw cycling and some measurements were done when samples had more time to dry, making them more hydrophobic. Static contact angle and roll-off angle at dewpoint were measured for the samples subjected to freeze-thaw cycling with the purpose of learning if dewpoint wetting would predict freeze resilience. As seen from Figure 26, the answer is generally yes, with notable exceptions being samples with 0 wt% TEOS. Without any binder, it is likely that the coatings are simply too weak. However, no direct strength measurement, such as tape peel, was done to confirm that.

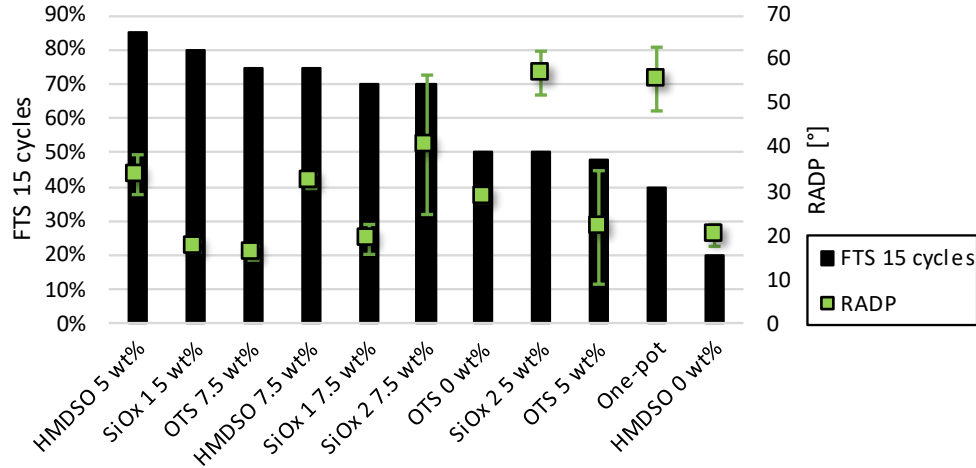


Figure 26: Correlation between survival, defined as the proportion of 10 μ l droplets sliding off the sample when tilting it to 90°, and the roll-off angle of 10 μ l droplets at dewpoint. SiOx 1 and 2 denotes 1 and 2 minutes of SiO_x treatment of the glass substrates respectively and wt% is the TEOS concentration.

Interestingly, while the WCA of pristine samples to some extent explains freeze-thaw durability, it does not give the whole picture. Likely, what happens is that when subjecting samples to temperatures below the dewpoint, water vapour enters the pores and condensates within the structure, regardless of water repellence. A thicker, sturdier hydrophobic layer, such as with the HMDSO samples, will give a more durable coating. To summarize the findings of the freeze-thaw cycling, regardless of hydrophobization technique, TEOS stood out as a predictor of freeze-thaw resilience, see Figure 27.

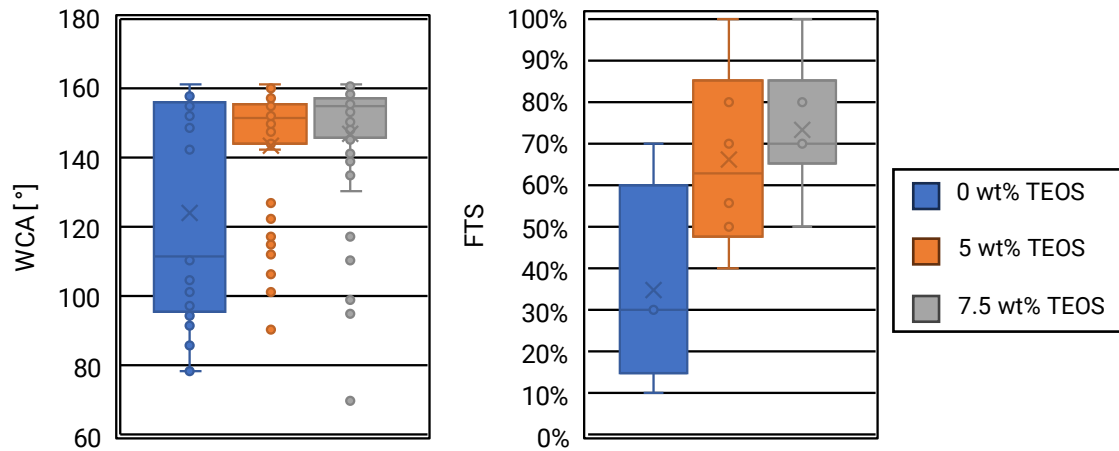


Figure 27: Water contact angle and freeze-thaw survival after 15 cycles by TEOS concentration, excluding one-pot and 10 wt% TEOS samples.

4.6 Ice adhesion results

Freezing with deionized water was repeated three times on the same spots on superhydrophobic samples. The test was particularly important for assessing hydrophobicity and durability, since prior to freezing, the samples were chilled below the dewpoint, allowing vapour to enter the microstructure. Due to instrument malfunctioning, ice adhesion results were limited from sample type GL510CO (5 wt% TEOS, 0.01 M HCl, not aged, dipped twice, calcined and hydrophobized by OTS), and 4 glass samples for reference. Table 7 shows the results from the ice adhesion tests of the SH samples. The glass measured an ice adhesion of 627 ± 96 kPa. Although limited to one sample type, the results are very encouraging with an ARF of 477-1670 and proves that the chilled water didn't wet the surface texture completely like in a Wenzel state prior to freezing, but on top of the surface texture, trapping air below, allowing for an extremely low ice adhesion.

Table 7: Results for ice adhesion measured as shear force. The samples were made with 5 wt% TEOS, calcined at 450°C and hydrophobized with OTS (GL510CO).

Sample nr	Ice adhesion [kPa]			Average all freezes
	1st freeze	2nd freeze	3rd freeze	
1	1.14	0.65	0.40	0.79±0.33
2	0.45	0.50	0.50	
3	0.25	0.60	2.59	
Mean each freeze	0.61±0.38	0.58±0.06	1.16±1.01	

4.7 Results from field test

The weather conditions for the field test were representative for the season in Stockholm and offered diverse range of freezing events. Figure 28 shows plots of temperature and precipitation for the test period. The temperature crossed freezing over 20 times for the duration. Precipitation came in the form of rain, wet and dry snow. Since the test location were a few kilometres from the SMHI weather station in central Stockholm, the actual field test conditions may have been slightly different than the official readings in Figure 28.

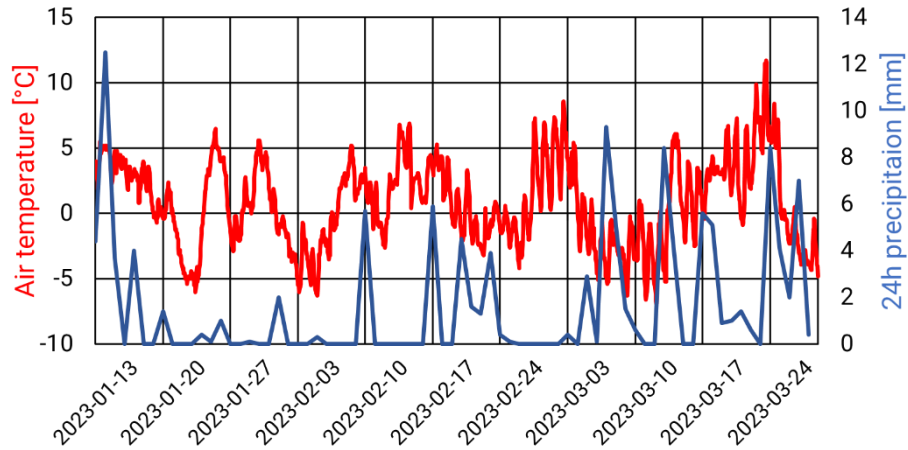


Figure 28: Temperature and precipitation data for Stockholm-Observatoriekullen, the closest weather station to the test location, for the field test duration. Web source: SMHI^{78,79}.

Pictures in Figure 29 from the field test show that the superhydrophobic sample did shed not only water but also snow and ice better than the reference at most of the conditions. Figure 29(a), from February 2nd, shows that the SH coating did help to clear snow after a snow event on February 1st. The night after, there was still snow on the reference while the superhydrophobic sample looked dry on the front side, Figure 29(b). After a cold night, less ice was present on the test sample than the reference as seen in Figure 29(c). After heavy snow at negative degrees between February 21st and 23rd, the sample cleared up faster than the reference, Figure 29(d)-(e). The superhydrophobic coating also proved to prevent or reduce the amount of frost formation, as evident from Figure 29(f)-(h). Figure 29(i) was photographed in milder weather and both the sample and the reference had cleared ice and snow. It is interesting to note that the water drops were bigger on the reference, likely because of it being more hydrophilic, although the contact angles could not be determined from the photograph. Figure 29(j) shows pictures after relatively large amounts of wet snow. While glass sheds wet snow well, the SH sample have areas totally clear from snow. The photographs in Figure 29(k) were taken the morning after a snowy night. Both samples are covered in snow. On the same afternoon, only a few water drops are present on the SH sample while the reference still holds a significant amount of frozen water, Figure 29(l).

Contact angle measurements were done after the field test and proved that the sample was still superhydrophobic but had signs of wear in the form of pinning in some spots, and very high roll-off angles, see Table 8. The sample was rinsed with IPA, ethanol and water and tested again. WCA was higher and RA lower after wash, indicating that the surface had been contaminated with dust.

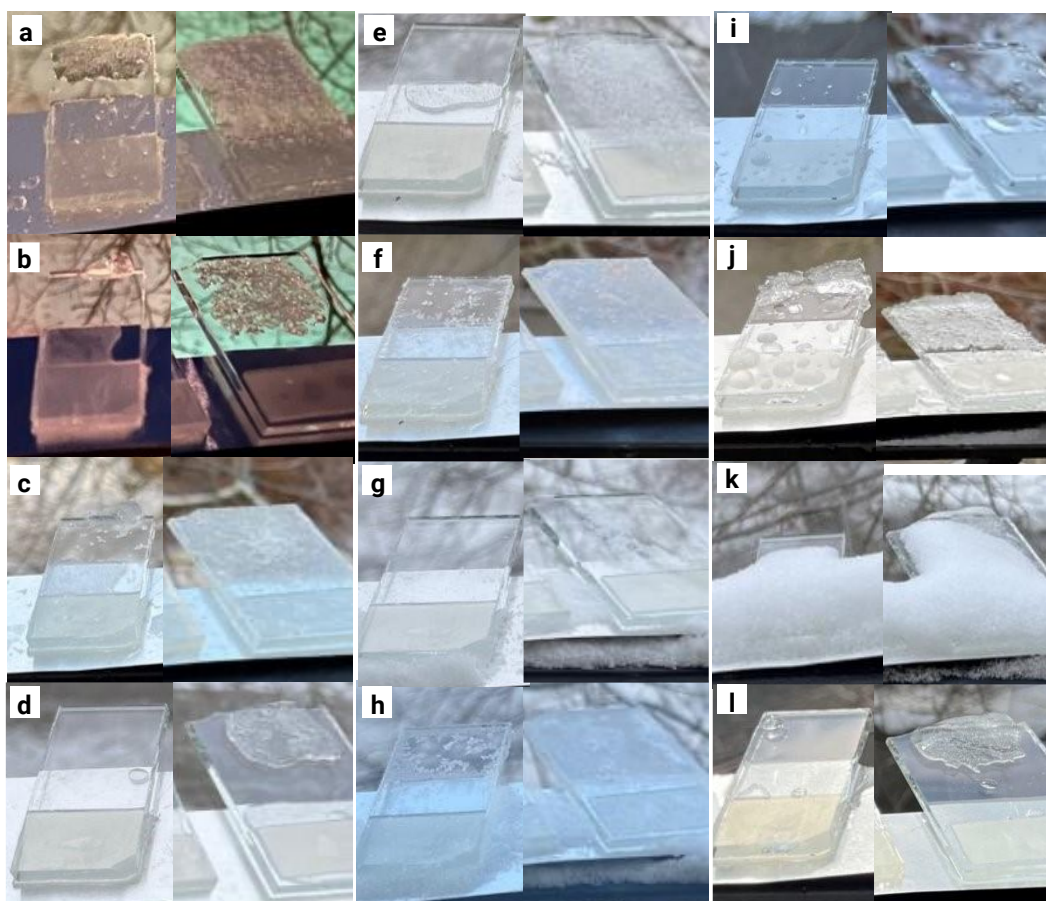


Figure 29: Pictures from field test of SH coated glass sample. For each group, the SH sample is on the left and glass reference on the right. (a) February 1st at 17:46, -2°C, (b) February 2nd at 18:20, -4°C, (c) February 3rd at 10:43, -2°C, (d) February 22nd at 16:14, -2°C, (e) February 25th at 14:57, 0°C, (f) March 7th at 08:25, -7°C, (g) March 8th at 14:24, -3°C, (h) March 9th at 07:41, -11°C, (i) March 9th at 14:54, -1°C, (j) March 25th at 17:15, 0°C, (k) March 28th at 10:26, -4°C, (l) March 28th at 15:50, -1°C.

Table 8: Contact angle and roll-off angles of superhydrophobic sample after the field test. 10 μ l droplet was used. Pinning means that the drop was stuck to the surface when table was tilted 90°.

	WCA [°]	RA [°]	Pinning
Before wash	149 \pm 7	59	1/3
After wash	153 \pm 3	32	2/4

The field test result is consistent with what was learned from the freeze-thaw cycling test, where samples showed decreased WCA and increased RA after testing, although there was great variation in between samples in durability.

5. Conclusions

In this thesis, transparent superhydrophobic coatings for solar cells have been synthesized and tested. Coatings were made using a sol-gel synthesis by dip-coating samples. Formulations were varied by several parameters: TEOS concentration, HCl concentration and aging. Also, different post-treatment temperatures, the hydrophobization method (self-assembly in desiccator and plasma), and the number of times dipping the samples were tested. Furthermore, 4 different one-pot formulations were tried. Lastly, SiO_x passivation barrier films of different thicknesses were applied to samples by plasma polymerization prior to dip-coating. Characterization was done by contact angle measurements with tilting at room temperature and at the dewpoint, UV-vis spectroscopy, tape peel tests, freeze-thaw cycling, XPS, SEM, profilometry, ice adhesion and a field test and gave a good overview of the prepared coatings parameters.

From the results, two factors stand out by having the largest impact on coating performance. Those are TEOS concentration and post-treatment temperature. Higher TEOS concentrations positively impacts durability as measured by tape peel strength and freeze-thaw cycling resilience, and result in improved water repellency. However, too high TEOS concentrations did affect transmittance negatively; thus, it was the reason for abandoning sols with 10 wt% TEOS. A cause for the lowered transmittance may be that a higher density of the film pushes the refractive index too high. Calcination of the coatings at 450°C improves their strength for all formulations and improves water repellency while retaining or possibly even improving transmittance. The latter may be due to removal of remaining unreacted organic compounds.

One issue that came up during the work was that during calcination at 450°C, sodium ions leaked from the glass and interfered with the OTS hydrophobization. Plasma polymerization was attempted to counter this by either applying a SiO_x barrier layer on to the glass before coating, or by replacing the hydrophobization step with OTS to instead use HMDSO to build a hydrophobic layer on the porous silica coating. So far, the effect of SiO_x in this regard is inconclusive, since XPS measurements on coated SiO_x were not done. The results from CA measurements, however, show that coatings on SiO_x were less hydrophobic than those on bare glass substrates. An interesting finding was that the most durable samples in the freeze-thaw test were hydrophobized with the plasma polymeric coatings, likely because of the much thicker, crosslinked layers than the ~1-2 nm SAMs from OTS.

Higher catalyst (HCl) amount improved the coating strength, at the cost of water repellence and transmittance. The condensation reaction (Eq. 12) may be promoted at higher HCl concentrations but it is difficult to say in what ways the gel structure is affected.

Another interesting finding was that by aging the sol to allow it to react prior to dip-coating, the coating properties were altered. Two protocols were used. The first one where sols with only minor amounts of alcohol (for dispersion of particles and TEOS) were aged for 24 hours and then diluting just prior to dip-coating. The other protocol was aging of a normally diluted sol for 4 days prior to dipping. The former aging protocol proved to have a negative impact on transmittance while improving coating strength slightly. The latter had less impact on it, but also a negative impact on coating strength, although water repellence was somewhat improved.

Several one-pot formulations were tried, allowing for making the coatings in one step. The motivation was two-fold. By removing the self-assembly step, the likelihood for adoption would increase and by having the hydrophobic groups in the bulk of the coating, it was believed to be potentially more durable, because it would still be hydrophobic after minor wear. Freeze-thaw cycling showed that the one-pot was not immune to wear. Although hydrophobic groups may still be present after loss of material, the density of hydrophobic groups may be lower. Another explanation may be that since for superhydrophobicity the surface structure is of key importance and that mechanical damage from the freeze and thaw cycles changed the surface features of the coatings in a way detrimental to the hydrophobicity. The transmittance was low for the one-pot with 9.5 wt% TEOS. By decreasing the TEOS concentration to 5 wt% and varying the OTS content at the price of hydrophobicity ($\text{WCA } 140 \pm 1^\circ$, slide-off failed), a one-pot coating with maximum TSW of 81.2% was achieved – still too low for the application.

The number of times each sample was dipped before curing had different effects depending on formulation. Most of the samples were dipped two times, to allow for better coverage. Those dipped once showed similar transmissivity and contact angles except for the one-pot coating, becoming significantly more transparent (TSW from 39% to 69%) from being dipped twice.

The over two months lasting winter field test in Stockholm showed that the superhydrophobic silica coating outperformed glass in shedding not only water, but also snow and ice, while having a TSW slightly better than glass, making the coating very attractive for the intended application on solar cells in cold locations.

Ice adhesion was evaluated for samples with a superhydrophobic coating made by 5 wt% TEOS and hydrophobized with OTS. The coating had a very low ice adhesion shear force of 0.79 ± 0.33 kPa compared to 627 ± 96 kPa for the glass reference, giving the coated sample an ARF of 477-1670. That is a very good result – ice formed on a solar cell cover glass with this coating would be greatly aided to fall off by gravity and wind, proving that the concept of ice repellent superhydrophobic silica coatings made by sol-gel synthesis is viable.

The work presented in this thesis is believed to contribute to the understanding of sol-gel silica-based superhydrophobic coatings with high transmittance and durability, and their anti-icing properties. This acquired knowledge can serve as a foundation for further studies. Potential paths for further research are discussed in the next section.

6. Future work

Further coating development work would primarily consist of improving the transmittance of the films (average TSW for all types excluding one-pot was $88.5 \pm 1.9\%$, very close to but slightly below the approximately 90% of low-iron float glass), their ice- and snowphobicity and their durability. For the transmittance, the refractive index of the coatings is currently unknown, but likely at 1.2 or more for the films with highest transmittance, since more TEOS lessen it while making the film denser. Ellipsometry could be used to determine the refractive index of the films. To gain a better understanding of the transmittance, the transmission spectrum could be measured using an integrating sphere spectrophotometer and going beyond 900 nm, at least to 1100 nm (the bandgap of silicon solar cells). Dipping speed, especially withdrawal speed, is important for both film thickness and structure and can be further tuned, as well as the number of dipping times. Varying the viscosity of the sols can be considered to affect film thickness. For all films produced within this thesis work, the same particles and amount (~ 2.5 wt% fumed silica, 14 nm nominal particle size) were used. Exploring these two parameters could be a part of future optimization of the transmittance. To improve ice- and snowphobicity and durability for the coatings, the hydrophobization would be reviewed. Focusing on SAMs, other options than OTS one would investigate are longer silanes, (OTS has eight carbon) or fatty acids, to improve the durability of the films. While their hydrophobicity and durability are unmatched, we are moving away from perfluorocarbons, a source of so called forever chemicals, excluding them as an option. XPS of calcined samples confirmed sodium ion leakage from the glass after calcination as the reason for issues with hydrophobization by SAMs from vapour phase. Further work would include optimization of the calcination protocol (potentially lower temperature and/or shorter time), rinsing and dealkalization, to reduce the amount of Na^+ interfering with the coating process. Finally, both ice adhesion testing and an expanded field test including more sample types using a selection based of contact angle and freeze-thaw cycling durability would give valuable information about the viability of the superhydrophobic coatings on solar cells in cold climate, and it is planned to undertake such investigations in the future.

7. Acknowledgements

Firstly, I would like to thank RISE Research Institutes of Sweden and Energimyndigheten (project nr 52472-1, dnr 2021-018755) for making this thesis possible. I would also like to express my sincere gratitude to the following people who have helped and supported me throughout this work:

My supervisors at RISE, Mikael Järn and Natalia Anna Wojas, for trusting me to carry out my thesis project with them, for being good instructors both in and outside the lab, for always being encouraging, and not the least for their unlimited patience helping me finish my thesis.

Mikael Sundin, who thoroughly taught me the contact angle instrument, the slip and peel tester and showed me how to do the ice adhesion test, as well as always being helpful in and about the lab. He was also responsible for the XPS and profilometry images.

My subject reader Jan Keller for all the invaluable input and help with my thesis.

My examiner Lena Klintberg for always being positive and taking her time answering all kinds of questions.

Kentth Johansson and Christina Makoundou for help with the plasma polymerization and sharing valuable insights into plasma theory and practice.

Mikael Järn for performing the field test.

Karin Hallstensson for helping me with the SEM images of my samples.

Wei Zhao for teaching me how to use the spectrophotometer and the sonicator.

Members of the SnowOff project not previously mentioned: Mattias Lindh, Anne Andersson, Stefan Karlsson and Alice Landmér for inspiring meetings and discussions.

All others at RISE for always being open, friendly, and welcoming.

Finally, a huge thanks to my wonderfully supportive wife Lovisa who made this possible and my son Oskar.

8. References

- (1) *Minskad elanvändning under 2022*. <https://www.energimyndigheten.se/nyhetsarkiv/2023/minskad-elanvandning-under-2022-i-sverige/> (accessed 2023-09-21).
- (2) *Nätanslutna solcellsanläggningar*. <https://www.energimyndigheten.se/statistik/den-officiella-statistiken/statistikprodukter/natanslutna-solcellsanlaggningar/> (accessed 2023-09-20).
- (3) Lindh, M.; Svedjeholm, M.; Granlund, A.; Petersson, J.; Malou Petersson, A. *Handbok För Nordlig Solek*; RISE Rapport; 2020.
- (4) Global SnowPack Available from EOC Geoservice. https://www.dlr.de/eoc/en/Portaldata/60/Resources/images/8_arch_2022/13_globalsnowpack/scd_2021.jpg (accessed 2023-08-25).
- (5) Andrews, R. W.; Pollard, A.; Pearce, J. M. The Effects of Snowfall on Solar Photovoltaic Performance. *Solar Energy* **2013**, *92*, 84–97. <https://doi.org/10.1016/j.solener.2013.02.014>.
- (6) Borreb, P.-O. A. Snow Adhesion Mitigation on Building Integrated Photovoltaics.
- (7) Andenæs, E.; Jelle, B. P.; Ramlo, K.; Kolås, T.; Selj, J.; Foss, S. E. The Influence of Snow and Ice Coverage on the Energy Generation from Photovoltaic Solar Cells. *Solar Energy* **2018**, *159*, 318–328. <https://doi.org/10.1016/j.solener.2017.10.078>.
- (8) Borrebæk, P. O. A.; Jelle, B. P.; Zhang, Z. Avoiding Snow and Ice Accretion on Building Integrated Photovoltaics – Challenges, Strategies, and Opportunities. *Solar Energy Materials and Solar Cells* **2020**, *206*. <https://doi.org/10.1016/j.solmat.2019.110306>.
- (9) Kreder, M. J.; Alvarenga, J.; Kim, P.; Aizenberg, J. Design of Anti-Icing Surfaces: Smooth, Textured or Slippery? *Nature Reviews Materials* **2016**, *1* (1). <https://doi.org/10.1038/natrevmats.2015.3>.
- (10) Alizadeh, A.; Yamada, M.; Li, R.; Shang, W.; Otta, S.; Zhong, S.; Ge, L.; Dhinojwala, A.; Conway, K. R.; Bahadur, V.; Vinciguerra, A. J.; Stephens, B.; Blohm, M. L. Dynamics of Ice Nucleation on Water Repellent Surfaces. *Langmuir* **2012**, *28* (6), 3180–3186. <https://doi.org/10.1021/la2045256>.
- (11) Liu, T. Q.; Sun, W.; Sun, X. Y.; Ai, H. R. Mechanism Study of Condensed Drops Jumping on Super-Hydrophobic Surfaces. *Colloids and Surfaces A: Physicochemical and Engineering Aspects* **2012**, *414*, 366–374. <https://doi.org/10.1016/j.colsurfa.2012.08.063>.
- (12) Manca, M.; Cannavale, A.; De Marco, L.; Aricò, A. S.; Cingolani, R.; Gigli, G. Durable Superhydrophobic and Antireflective Surfaces by Trimethylsilanized Silica Nanoparticles-Based Sol-Gel Processing. *Langmuir* **2009**, *25* (11), 6357–6362. <https://doi.org/10.1021/la804166t>.
- (13) Agustín-Sáenz, C.; Machado, M.; Nohava, J.; Yurrita, N.; Sanz, A.; Brizuela, M.; Zubillaga, O.; Tercjak, A. Mechanical Properties and Field Performance of Hydrophobic Antireflective Sol-Gel Coatings on the Cover Glass of Photovoltaic Modules. *Solar Energy Materials and Solar Cells* **2020**, *216*. <https://doi.org/10.1016/j.solmat.2020.110694>.
- (14) Celia, E.; Darmanin, T.; Taffin de Givenchy, E.; Amigoni, S.; Guittard, F. Recent Advances in Designing Superhydrophobic Surfaces. *Journal of Colloid and Interface Science* **2013**, *402*, 1–18. <https://doi.org/10.1016/j.jcis.2013.03.041>.
- (15) Quéré, D. Wetting and Roughness. *Annual Review of Materials Research* **2008**, *38*, 71–99. <https://doi.org/10.1146/annurev.matsci.38.060407.132434>.
- (16) Nguyen-Tri, P.; Tran, H. N.; Plamondon, C. O.; Tuduri, L.; Vo, D. V. N.; Nanda, S.; Mishra, A.; Chao, H. P.; Bajpai, A. K. Recent Progress in the Preparation, Properties and Applications of Superhydrophobic Nano-Based Coatings and Surfaces: A Review. *Progress in Organic Coatings* **2019**, *132*, 235–256. <https://doi.org/10.1016/j.porgcoat.2019.03.042>.
- (17) Marmur, A. Soft Contact: Measurement and Interpretation of Contact Angles. *Soft Matter* **2006**, *2* (1), 12–17. <https://doi.org/10.1039/b514811c>.
- (18) Järn, M. Influence of Topography and Surface Chemistry on the Wetting Properties of TiO₂-Based Ceramic Coatings, Åbo Akademi - Åbo Akademi University, 2010. <https://www.doria.fi/handle/10024/66623>.
- (19) Erbil, H. Y. The Debate on the Dependence of Apparent Contact Angles on Drop Contact Area or Three-Phase Contact Line: A Review. *Surface Science Reports* **2014**, *69* (4), 325–365. <https://doi.org/10.1016/j.surfrep.2014.09.001>.

- (20) Bartell, F. E.; Shepard, J. W. The Effect of Surface Roughness on Apparent Contact Angles and on Contact Angle Hysteresis. I. The System Paraffin–Water–Air. *J. Phys. Chem.* **1953**, *57* (2), 211–215. <https://doi.org/10.1021/j150503a017>.
- (21) Extrand, C. W. Contact Angles and Hysteresis on Surfaces with Chemically Heterogeneous Islands. *Langmuir* **2003**, *19* (9), 3793–3796. <https://doi.org/10.1021/la0268350>.
- (22) Gao, L.; McCarthy, T. J. How Wenzel and Cassie Were Wrong. *Langmuir* **2007**, *23* (7), 3762–3765. <https://doi.org/10.1021/la062634a>.
- (23) Marmur, A.; Bittoun, E. When Wenzel and Cassie Are Right: Reconciling Local and Global Considerations. *Langmuir* **2009**, *25* (3), 1277–1281. <https://doi.org/10.1021/la802667b>.
- (24) Latthe, S. S.; Imai, H.; Ganesan, V.; Venkateswara Rao, A. Porous Superhydrophobic Silica Films by Sol-Gel Process. *Microporous and Mesoporous Materials* **2010**, *130* (1–3), 115–121. <https://doi.org/10.1016/j.micromeso.2009.10.020>.
- (25) Mozumder, M. S.; Mourad, A. H. I.; Pervez, H.; Surkatti, R. Recent Developments in Multifunctional Coatings for Solar Panel Applications: A Review. *Solar Energy Materials and Solar Cells* **2019**, *189*, 75–102. <https://doi.org/10.1016/j.solmat.2018.09.015>.
- (26) McHale, G. All Solids, Including Teflon, Are Hydrophilic (To Some Extent), But Some Have Roughness Induced Hydrophobic Tendencies. *Langmuir* **2009**, *25* (13), 7185–7187. <https://doi.org/10.1021/la900597a>.
- (27) Gao, L.; McCarthy, T. J. Wetting 101°. *Langmuir* **2009**, *25* (24), 14105–14115. <https://doi.org/10.1021/la902206c>.
- (28) Furmidge, C. G. L. Studies at Phase Interfaces. I. The Sliding of Liquid Drops on Solid Surfaces and a Theory for Spray Retention. *Journal of Colloid Science* **1962**, *17* (4), 309–324. [https://doi.org/10.1016/0095-8522\(62\)90011-9](https://doi.org/10.1016/0095-8522(62)90011-9).
- (29) Callister, W. D., Jr; Rethwisch, D. G. Light Interactions with Solids. In *Materials Science and Engineering: An Introduction*; Wiley: Hoboken, 2018; pp 754–754.
- (30) Karthik, D.; Pendse, S.; Sakthivel, S.; Ramasamy, E.; Joshi, S. V. High Performance Broad Band Antireflective Coatings Using a Facile Synthesis of Ink-Bottle Mesoporous MgF₂ Nanoparticles for Solar Applications. *Solar Energy Materials and Solar Cells* **2017**, *159*, 204–211. <https://doi.org/10.1016/j.solmat.2016.08.007>.
- (31) Zäll, E.; Järn, M.; Karlsson, S.; Tryggesson, H.; Tuominen, M.; Sundin, M.; Wågberg, T. Aerosol-Based Deposition of Broadband Antireflective Silica Coating with Closed Mesoporous Structure. *Solar Energy Materials and Solar Cells* **2023**, *250*. <https://doi.org/10.1016/j.solmat.2022.112078>.
- (32) Shanmugam, N.; Pugazhendhi, R.; Elavarasan, R. M.; Kasiviswanathan, P.; Das, N. Anti-Reflective Coating Materials: A Holistic Review from PV Perspective. *Energies* **2020**, *13* (10). <https://doi.org/10.3390/en13102631>.
- (33) Jönsson, U.; Olofsson, G.; Malmqvist, M.; Rönnberg, I. PREPARATION AND CHARACTERIZATION 117 CHEMICAL VAPOUR DEPOSITION OF SILANES*; Thin Solid Films; 1985; Vol. 124, pp 117–123.
- (34) Bravo, J.; Zhai, L.; Wu, Z.; Cohen, R. E.; Rubner, M. F. Transparent Superhydrophobic Films Based on Silica Nanoparticles. *Langmuir* **2007**, *23* (13), 7293–7298. <https://doi.org/10.1021/la070159q>.
- (35) Li, X.; Du, X.; He, J. Self-Cleaning Antireflective Coatings Assembled from Peculiar Mesoporous Silica Nanoparticles. *Langmuir* **2010**, *26* (16), 13528–13534. <https://doi.org/10.1021/la1016824>.
- (36) Xu, L.; Karunakaran, R. G.; Guo, J.; Yang, S. Transparent, Superhydrophobic Surfaces from One-Step Spin Coating of Hydrophobic Nanoparticles. *ACS Applied Materials and Interfaces* **2012**, *4* (2), 1118–1125. <https://doi.org/10.1021/am201750h>.
- (37) Li, X.; He, J.; Liu, W. Broadband Anti-Reflective and Water-Repellent Coatings on Glass Substrates for Self-Cleaning Photovoltaic Cells. *Materials Research Bulletin* **2013**, *48* (7), 2522–2528. <https://doi.org/10.1016/j.materresbull.2013.03.017>.
- (38) Mahadik, D. B.; Lakshmi, R. V.; Barshilia, H. C. High Performance Single Layer Nano-Porous Antireflection Coatings on Glass by Sol-Gel Process for Solar Energy Applications. *Solar Energy Materials and Solar Cells* **2015**, *140*, 61–68. <https://doi.org/10.1016/j.solmat.2015.03.023>.
- (39) Smått, J.-Henrik. *Hierarchically Porous Silica, Carbon, and Metal Oxide Monoliths: Synthesis and Characterization*; Åbo Akademi University, 2006.
- (40) Faustini, M.; Louis, B.; Albouy, P. A.; Kuemmel, M.; Grosso, D. Preparation of Sol–Gel Films by Dip-Coating in Extreme Conditions. *J. Phys. Chem. C* **2010**, *114* (17), 7637–7645. <https://doi.org/10.1021/jp9114755>.

- (41) Langmuir, I. Oscillations in Ionized Gases. *Proc Natl Acad Sci U S A* **1928**, *14* (8), 627–637. <https://doi.org/10.1073/pnas.14.8.627>.
- (42) Bittencourt, J. A. *Fundamentals of Plasma Physics*, 3rd ed.; Springer: New York, 2004.
- (43) Ye, Z.; Zhao, L.; Nikiforov, A.; Giraudon, J.-M.; Chen, Y.; Wang, J.; Tu, X. A Review of the Advances in Catalyst Modification Using Nonthermal Plasma: Process, Mechanism and Applications. *Advances in Colloid and Interface Science* **2022**, *308*, 102755. <https://doi.org/10.1016/j.cis.2022.102755>.
- (44) Munief, W. M.; Heib, F.; Hempel, F.; Lu, X.; Schwartz, M.; Pachauri, V.; Hempelmann, R.; Schmitt, M.; Ingebrandt, S. Silane Deposition via Gas-Phase Evaporation and High-Resolution Surface Characterization of the Ultrathin Siloxane Coatings. *Langmuir* **2018**, *34* (35), 10217–10229. <https://doi.org/10.1021/acs.langmuir.8b01044>.
- (45) Borrebæk, P. O. A.; Rønneberg, S.; Jelle, B. P.; Klein-Paste, A.; Zhang, Z.; He, J. A Framework for Classification of Snow- and Icephobicity. *Journal of Adhesion Science and Technology* **2021**, *35* (10), 1087–1098. <https://doi.org/10.1080/01694243.2020.1834286>.
- (46) Makkonen, L. Ice Adhesion - Theory, Measurements and Countermeasures. *Journal of Adhesion Science and Technology* **2012**, *26* (4–5), 413–445. <https://doi.org/10.1163/016942411X574583>.
- (47) Work, A.; Lian, Y. A Critical Review of the Measurement of Ice Adhesion to Solid Substrates. *Progress in Aerospace Sciences* **2018**, *98*, 1–26. <https://doi.org/10.1016/j.paerosci.2018.03.001>.
- (48) Rønneberg, S.; He, J.; Zhang, Z. The Need for Standards in Low Ice Adhesion Surface Research: A Critical Review. *Journal of Adhesion Science and Technology* **2020**, *34* (3), 319–347. <https://doi.org/10.1080/01694243.2019.1679523>.
- (49) Rønneberg, S.; Zhuo, Y.; Laforte, C.; He, J.; Zhang, Z. Interlaboratory Study of Ice Adhesion Using Different Techniques. *Coatings* **2019**, *9* (10). <https://doi.org/10.3390/coatings9100678>.
- (50) Rønneberg, S.; Laforte, C.; Volat, C.; He, J.; Zhang, Z. The Effect of Ice Type on Ice Adhesion. *AIP Advances* **2019**, *9* (5), 055304. <https://doi.org/10.1063/1.5086242>.
- (51) Meuler, A. J.; Smith, J. D.; Varanasi, K. K.; Mabry, J. M.; McKinley, G. H.; Cohen, R. E. Relationships between Water Wettability and Ice Adhesion. *ACS Appl. Mater. Interfaces* **2010**, *2* (11), 3100–3110. <https://doi.org/10.1021/am1006035>.
- (52) Andersson, P. O.; Jelle, B. P.; Zhang, Z. Passive Snow Repulsion: A State-of-the-Art Review Illuminating Research Gaps and Possibilities; Elsevier Ltd, 2017; Vol. 132, pp 423–428. <https://doi.org/10.1016/j.egypro.2017.09.650>.
- (53) Kako, T.; Nakajima, A.; Irie, H.; Kato, Z.; Uematsu, K.; Watanabe, T.; Hashimoto, K. *Adhesion and Sliding of Wet Snow on a Super-Hydrophobic Surface with Hydrophilic Channels*.
- (54) Fillion, R. M.; Riahi, A. R.; Edrissy, A. A Review of Icing Prevention in Photovoltaic Devices by Surface Engineering. *Renewable and Sustainable Energy Reviews* **2014**, *32*, 797–809. <https://doi.org/10.1016/j.rser.2014.01.015>.
- (55) Jung, S.; Dorrestijn, M.; Raps, D.; Das, A.; Megaridis, C. M.; Poulikakos, D. Are Superhydrophobic Surfaces Best for Icephobicity? *Langmuir* **2011**, *27* (6), 3059–3066. <https://doi.org/10.1021/la104762g>.
- (56) Andersson, P.-O.; Petter Jelle, B.; Zhang, Z.; Gao, T.; Ng, S.; Selj, J.; Foss, S. E.; Marstein, E. S.; Kolås, T. *A Review of Possible Pathways for Avoiding Snow and Ice Formation on Building Integrated Photovoltaics*.
- (57) Dhyani, A.; Pike, C.; Braid, J. L.; Whitney, E.; Burnham, L.; Tuteja, A. Facilitating Large-Scale Snow Shedding from In-Field Solar Arrays Using Icephobic Surfaces with Low-Interfacial Toughness. *Advanced Materials Technologies* **2022**, *7* (5). <https://doi.org/10.1002/admt.202101032>.
- (58) Hejazi, V.; Sobolev, K.; Nosonovsky, M. From Superhydrophobicity to Icephobicity: Forces and Interaction Analysis. *Scientific Reports* **2013**, *3*. <https://doi.org/10.1038/srep02194>.
- (59) Gao, L.; He, J. A Facile Dip-Coating Approach Based on Three Silica Sols to Fabrication of Broadband Antireflective Superhydrophobic Coatings. *Journal of Colloid and Interface Science* **2013**, *400*, 24–30. <https://doi.org/10.1016/j.jcis.2013.03.013>.
- (60) Lafuma, A.; Quéré, D. Superhydrophobic States. *Nature Mater* **2003**, *2* (7), 457–460. <https://doi.org/10.1038/nmat924>.
- (61) Wong, T. S.; Kang, S. H.; Tang, S. K. Y.; Smythe, E. J.; Hatton, B. D.; Grinthal, A.; Aizenberg, J. Bioinspired Self-Repairing Slippery Surfaces with Pressure-Stable Omniphobicity. *Nature* **2011**, *477* (7365), 443–447. <https://doi.org/10.1038/nature10447>.
- (62) Kim, P.; Wong, T.-S.; Alvarenga, J.; Kreder, M. J.; Adorno-Martinez, W. E.; Aizenberg, J. Liquid-Infused Nanostructured Surfaces with Extreme Anti-Ice and Anti-Frost Performance. *ACS Nano* **2012**, *6* (8), 6569–6577. <https://doi.org/10.1021/nn302310q>.

- (63) Zhuo, Y.; Wang, F.; Xiao, S.; He, J.; Zhang, Z. One-Step Fabrication of Bioinspired Lubricant-Regenerable Icephobic Slippery Liquid-Infused Porous Surfaces. *ACS Omega* **2018**, *3* (8), 10139–10144. <https://doi.org/10.1021/acsomega.8b01148>.
- (64) Rykaczewski, K.; Anand, S.; Subramanyam, S. B.; Varanasi, K. K. Mechanism of Frost Formation on Lubricant-Impregnated Surfaces. *Langmuir* **2013**, *29* (17), 5230–5238. <https://doi.org/10.1021/la400801s>.
- (65) Yeong, Y. H.; Milionis, A.; Loth, E.; Sokhey, J. Self-Lubricating Icephobic Elastomer Coating (SLIC) for Ultralow Ice Adhesion with Enhanced Durability. *Cold Regions Science and Technology* **2018**, *148*, 29–37. <https://doi.org/10.1016/j.coldregions.2018.01.005>.
- (66) Zhu, L.; Xue, J.; Wang, Y.; Chen, Q.; Ding, J.; Wang, Q. Ice-Phobic Coatings Based on Silicon-Oil-Infused Polydimethylsiloxane. *ACS Appl. Mater. Interfaces* **2013**, *5* (10), 4053–4062. <https://doi.org/10.1021/am400704z>.
- (67) Tao, C.; Li, X.; Liu, B.; Zhang, K.; Zhao, Y.; Zhu, K.; Yuan, X. Highly Icephobic Properties on Slippery Surfaces Formed from Polysiloxane and Fluorinated POSS. *Progress in Organic Coatings* **2017**, *103*, 48–59. <https://doi.org/10.1016/j.porgcoat.2016.11.018>.
- (68) Golovin, K.; Tuteja, A. *A Predictive Framework for the Design and Fabrication of Icephobic Polymers*; 2017. <http://advances.sciencemag.org/>.
- (69) Wang, Y.; He, J. Fabrication of Ultra-Smooth Hybrid Thin Coatings towards Robust, Highly Transparent, Liquid-Repellent and Antismudge Coatings. *Journal of Colloid and Interface Science* **2021**, *594*, 781–790. <https://doi.org/10.1016/j.jcis.2021.03.077>.
- (70) Johansson, K. S. Gas Barrier Properties of Plasma-Deposited Coatings – Substrate Effects. In *Polymer surface modification: relevance to adhesion. Volume 2*; CRC Press, Taylor & Francis Group: Boca Raton, 2000; Vol. 2.
- (71) ASTM Standard G173, Standard Tables for Reference Solar Spectral Irradiances: Direct Normal and Hemispherical on 39 Tilted Surface, ASTM International, 2020 [Online]. <https://www.astm.org/> (accessed 2023-08-18).
- (72) Heydari, G.; Thormann, E.; Järn, M.; Tyrode, E.; Claesson, P. M. Hydrophobic Surfaces: Topography Effects on Wetting by Supercooled Water and Freezing Delay. *Journal of Physical Chemistry C* **2013**, *117* (42), 21752–21762. <https://doi.org/10.1021/jp404396m>.
- (73) IEC 62108:2016 - Concentrator Photovoltaic (CPV) Modules and Assemblies – Design Qualification and Type Approval. *IEC* **2016**.
- (74) Mayeen, A.; Shaji, L. K.; Nair, A. K.; Kalarikkal, N. Morphological Characterization of Nanomaterials. In *Characterization of Nanomaterials*; Elsevier, 2018; pp 335–364. <https://doi.org/10.1016/B978-0-08-101973-3.00012-2>.
- (75) Zhao, X.; Soper, S. A.; Murphy, M. C. A High-Adhesion Binding Strategy for Silica Nanoparticle-Based Superhydrophobic Coatings. *Colloids and Surfaces A: Physicochemical and Engineering Aspects* **2021**, *625*. <https://doi.org/10.1016/j.colsurfa.2021.126810>.
- (76) Dalbe, M.-J.; Cortet, P.-P.; Ciccotti, M.; Vanel, L.; Santucci, S. Multiscale Stick-Slip Dynamics of Adhesive Tape Peeling. *Phys. Rev. Lett.* **2015**, *115* (12), 128301. <https://doi.org/10.1103/PhysRevLett.115.128301>.
- (77) Thoroddsen, S. T.; Nguyen, H. D.; Takehara, K.; Etoh, T. G. Stick-Slip Substructure in Rapid Tape Peeling. *Phys. Rev. E* **2010**, *82* (4), 046107. <https://doi.org/10.1103/PhysRevE.82.046107>.
- (78) *Ladda ner meteorologiska observationer | SMHI*. <https://www.smhi.se/data/meteorologi/ladda-ner-meteorologiska-observationer/#param=airtemperatureInstant,stations=core,stationid=98210> (accessed 2023-09-12).
- (79) *Ladda ner meteorologiska observationer | SMHI*. <https://www.smhi.se/data/meteorologi/ladda-ner-meteorologiska-observationer/#param=precipitation24HourSum,stations=core,stationid=98230> (accessed 2023-09-12).

9. APPENDICES

APPENDIX A – SAMPLE NOMENCLATURE

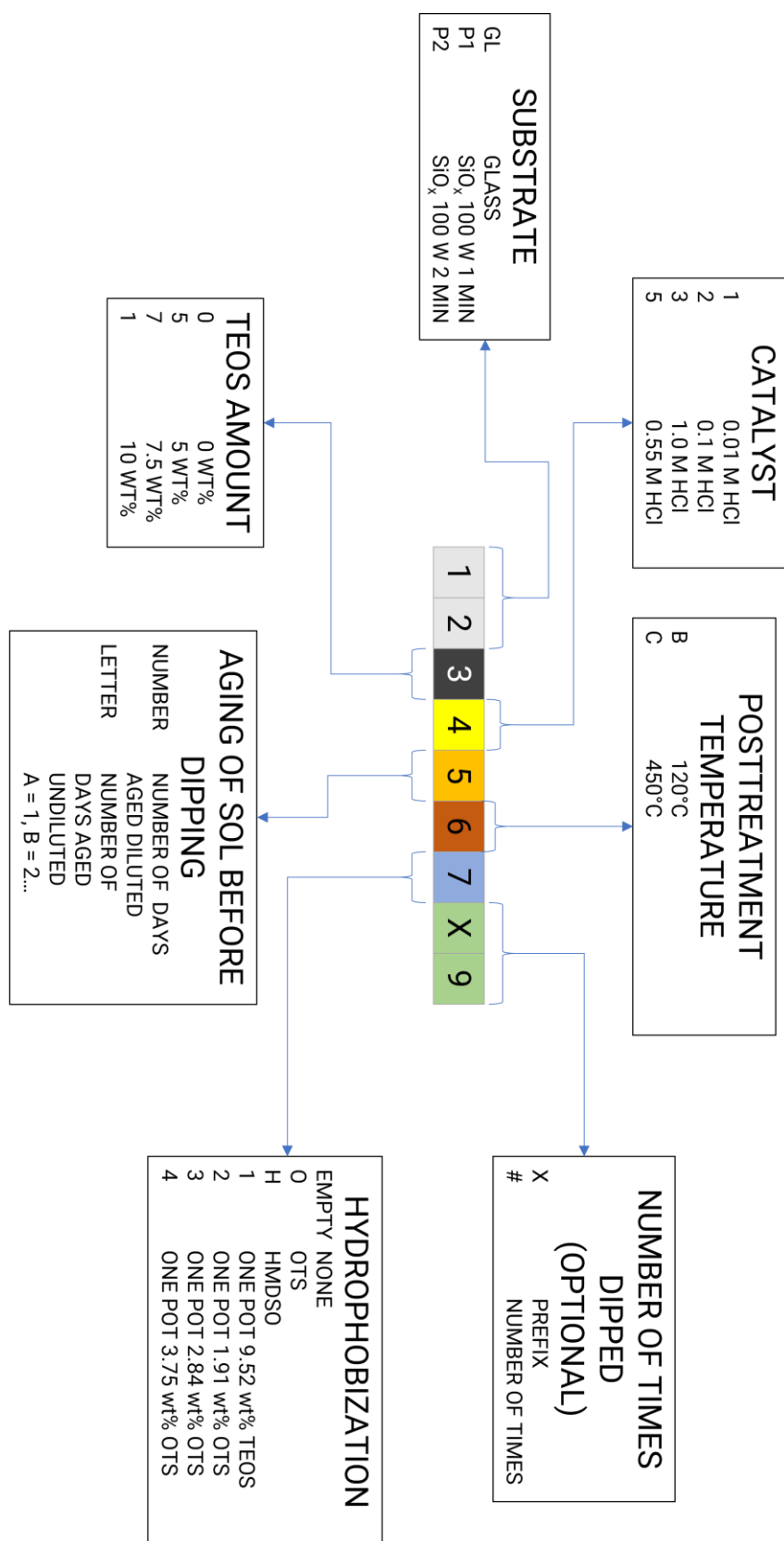


Figure A.I: Depiction of the sample type encoding used in this thesis.

APPENDIX B – PROFILOMETRY PLOTS

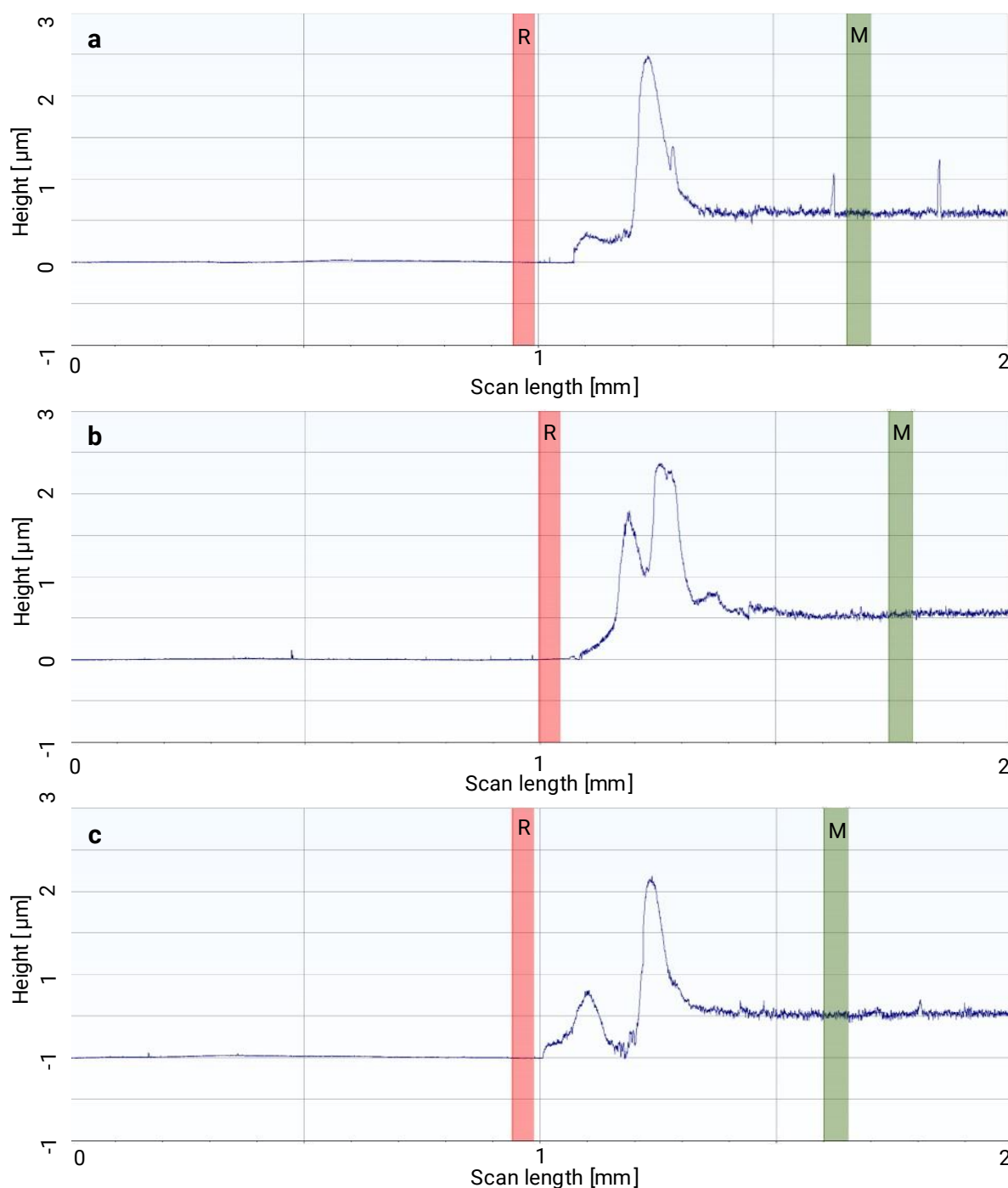


Figure B.I: Line profilometry plots for sample type GL710CO, 7.5 wt% TEOS, dipped two times. (a), (b) and (c) are profiles for longitudinal lines separated by 1 mm. On the left, where R (red) is placed is a part of the substrate profile and to the right where M (green) is placed is a part of the profile for the coating. Between R and M is the edge, where the coating is thicker. The measured height differences between R and M for (a), (b), and (c) is 595 nm, 543 nm, and 498 nm respectively.

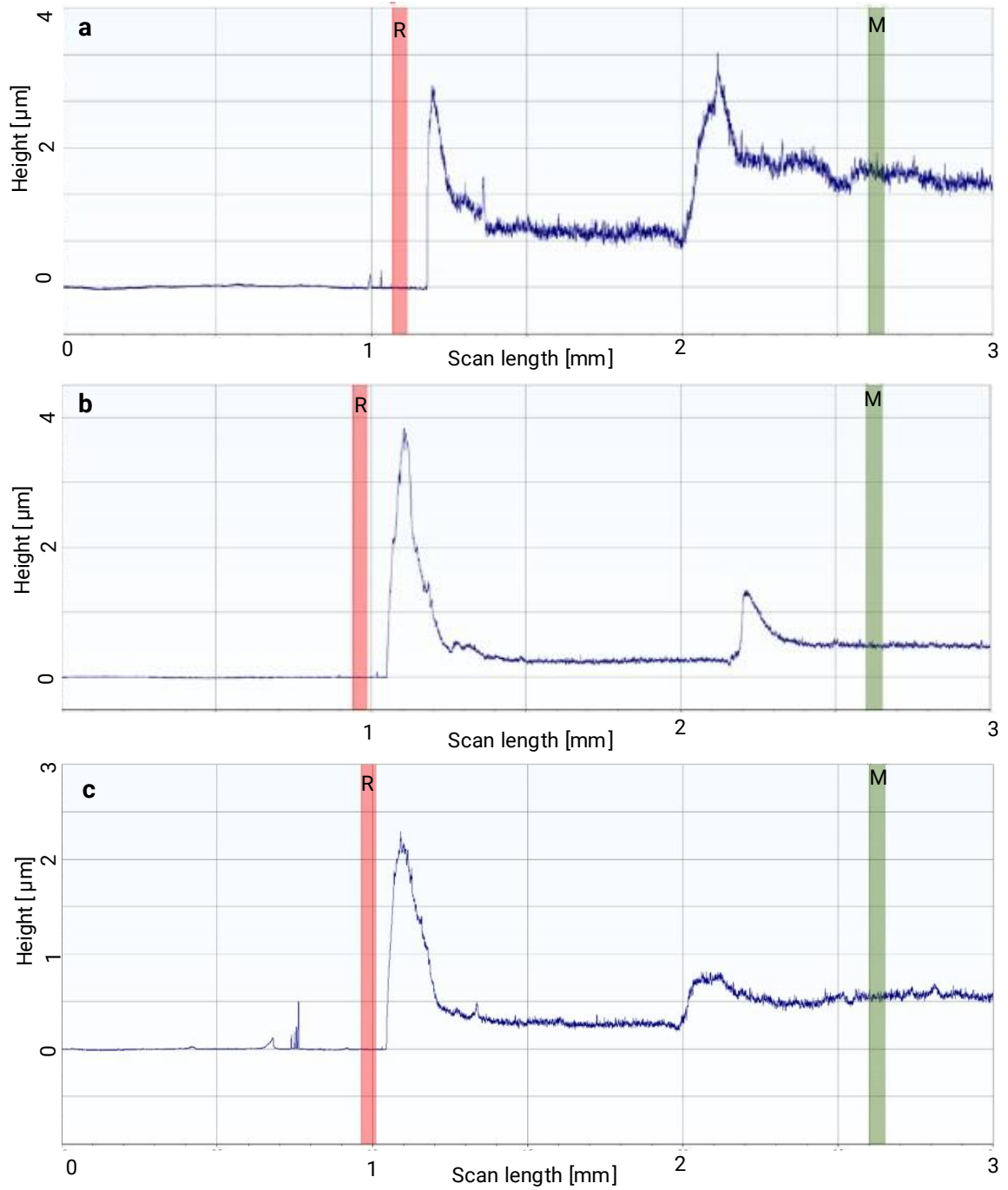


Figure B.II: Line profilometry plots for sample type GL110CO, 10 wt% TEOS, dipped two times. (a), (b) and (c) are profiles for longitudinal lines separated by 1 mm. On the left, where R (red) is placed is an area of the substrate profile and to the right where M (green) is placed is an area of the profile for the coating. Between R and M is the edge, where the coating is thicker. The measured height differences between R and M for (a), (b), and (c) is 498 nm, 489 nm, and 554 nm respectively. It's clear that the samples have been dipped two times since the overlap is not perfect.

APPENDIX C – TABLES

Table I: Solar weighted transmittance (based on Eq. 13). (*) One-pot coatings are formulated differently. (**) for aging, refer to Appendix A.

SAMPLE TYPE	FORMU- LATION	SUBSTRATE	TEOS [wt%]	HCl [M]	AGING (**)	DIP NR	POST- TREATMENT [°C]	HP METHOD	TSW [%]
GL030B	0C	Glass	0	1	no	2	120	-	85.8
GL030C	0C	Glass	0	1	no	2	450	-	91.1
GL030CH	0C	Glass	0	1	no	2	450	HMDSO	89.7
GL110CO	3A	Glass	10	0.01	no	2	450	OTS	84.7±1.4
GL110COX1	3A	Glass	10	0.01	no	1	450	OTS	83.8
GL130B1	O1	Glass	9.8	*	no	2	120	One pot	69.0
GL130B1X1	O1	Glass	9.8	*	no	1	120	One pot	38.7
GL510BO	1A	Glass	5	*	no	2	120	OTS	89.2±0.2
GL510B2	O52	Glass	5	*	no	2	120	One pot	81.6
GL510B3	O53	Glass	5	*	no	2	120	One pot	77.5
GL510B4	O54	Glass	5	*	no	2	120	One pot	73.0
GL510CO	1A	Glass	5	0.01	no	2	450	OTS	91.4±0.1
GL520C	1B	Glass	5	0.1	no	2	450	-	90.1
GL524BO	1B	Glass	5	0.1	4	2	120	OTS	90.0
GL524CO	1B	Glass	5	0.1	4	2	450	OTS	90.2
GL52AB	1B	Glass	5	0.1	A	2	120	-	90.0±0.1
GL52AC	1B	Glass	5	0.1	A	2	450	-	89.4±0.4
GL530C	1C	Glass	5	1	no	2	450	-	90.4
GL530CH	1C	Glass	5	1	no	2	450	HMDSO	86.2
GL534BO	1C	Glass	5	1	4	2	120	OTS	90.3
GL534CO	1C	Glass	5	1	4	2	450	OTS	90.1
GL53AB	1C	Glass	5	1	A	2	120	-	90.0±0.1
GL53AC	1C	Glass	5	1	A	2	450	-	88.9±0.1
GL710CO	2A	Glass	7.5	0.01	no	2	450	OTS	88.9±1.2
GL710COX1	2A	Glass	7.5	0.01	no	1	450	OTS	88.0
GL720C	2B	Glass	7.5	0.1	no	2	450	-	89.1
GL724BO	2B	Glass	7.5	0.1	4	2	120	OTS	91.5
GL724CO	2B	Glass	7.5	0.1	4	2	450	OTS	88.8
GL730C	2C	Glass	7.5	1	no	2	450	-	89.2
GL730CH	2C	Glass	7.5	1	no	2	450	HMDSO	88.5
GL734BO	2C	Glass	7.5	1	4	2	120	OTS	88.3
GL734CO	2C	Glass	7.5	1	4	2	450	OTS	88.0
GL75AB	2D	Glass	7.5	0.55	A	2	120	-	86.8±0.0
GL75AC	2D	Glass	7.5	0.55	A	2	450	-	86.5±0.1
P1	-	SiO _x 1 min	-	-	-	-	-	-	90.4
P1530C	1C	SiO _x 1 min	5	1	no	2	450	-	89.3
P1730C	2C	SiO _x 1 min	7.5	1	no	2	450	-	88.7
P2	-	SiO _x 2 min	-	-	-	-	-	-	92.6
P2530C	1C	SiO _x 2 min	5	1	no	2	450	-	90.7
P2730C	2C	SiO _x 2 min	7.5	1	no	2	450	-	88.9

Table II: Results from survey spectrum of coated Si wafer post-treated at 120°C.

Quantification Report								
/c=/data/MSU_data/120C_coated_Si_wafer.dset						Mon Apr 3 12:29:32 2023		
State : Angle Name : 120C coated Si wafer								
Peak	Type	Position BE (eV)	FWHM (eV)	Raw Area (cps eV)	RSF	Atomic Mass	Atomic Conc %	Mass Conc %
O 1s	Reg	532.000	3.146	2446682.2	0.780	15.999	69.53	58.42
C 1s	Reg	285.000	4.082	58391.9	0.278	12.011	3.98	2.51
Si 2p	Reg	103.000	3.220	505874.3	0.328	28.086	26.49	33.07

Table III: Results from survey spectrum of coated Si wafer post-treated at 450°C.

State : Angle Name : 450C coated Si wafer								
Peak	Type	Position BE (eV)	FWHM (eV)	Raw Area (cps eV)	RSF	Atomic Mass	Atomic Conc %	Mass Conc %
O 1s	Reg	533.300	3.426	2661705.8	0.780	15.999	73.75	62.20
C 1s	Reg	285.300	4.062	19063.2	0.278	12.011	1.26	0.80
Si 2p	Reg	104.300	3.396	483605.8	0.328	28.086	24.99	37.00

Table IV: Results from detail spectra of coated glass post-treated at 120°C.

State : Angle Name : 120C coated								
Peak	Type	Position BE (eV)	FWHM (eV)	Raw Area (cps eV)	RSF	Atomic Mass	Atomic Conc %	Mass Conc %
Na 1s	Reg	1072.450	0.251	393.8	1.685	22.990	0.01	0.02
O 1s	Reg	531.800	2.125	1009719.7	0.780	15.999	71.44	60.82
C 1s	Reg	285.000	3.644	22428.7	0.278	12.011	4.08	2.61
Si 2p	Reg	103.500	2.081	172016.2	0.328	28.086	24.46	36.56
State : Angle Name : 120C coated pt.2								
Peak	Type	Position BE (eV)	FWHM (eV)	Raw Area (cps eV)	RSF	Atomic Mass	Atomic Conc %	Mass Conc %
Na 1s	Reg	1071.850	0.290	676.4	1.685	22.990	0.03	0.03
O 1s	Reg	532.900	1.801	1004944.0	0.780	15.999	71.12	60.39
C 1s	Reg	285.000	3.342	22126.9	0.278	12.011	4.02	2.56
Si 2p	Reg	103.600	1.972	174651.7	0.328	28.086	24.84	37.02

Table V: Results from detail spectra of coated glass post-treated at 450°C.

State : Angle Name : 450C coated								
Peak	Type	Position BE (eV)	FWHM (eV)	Raw Area (cps eV)	RSF	Atomic Mass	Atomic Conc %	Mass Conc %
Na 1s	Reg	1072.050	2.386	15588.1	1.685	22.990	0.57	0.69
O 1s	Reg	533.000	1.921	1026352.7	0.780	15.999	71.82	60.19
C 1s	Reg	285.000	1.985	9932.8	0.278	12.011	1.79	1.12
Si 2p	Reg	103.600	2.022	183670.7	0.328	28.086	25.82	38.00
State : Angle Name : 450 coated pt.2								
Peak	Type	Position BE (eV)	FWHM (eV)	Raw Area (cps eV)	RSF	Atomic Mass	Atomic Conc %	Mass Conc %
Na 1s	Reg	1071.750	2.285	13691.9	1.685	22.990	0.54	0.65
O 1s	Reg	533.000	2.404	935373.2	0.780	15.999	70.80	58.84
C 1s	Reg	284.900	2.052	7960.3	0.278	12.011	1.55	0.97
Si 2p	Reg	103.400	2.066	178258.8	0.328	28.086	27.11	39.55

Table VI: Results of survey spectra of uncoated glass heated to 120°C.

State : Angle Name : 120C uncoated								
Peak	Type	Position BE (eV)	FWHM (eV)	Raw Area (cps eV)	RSF	Atomic Mass	Atomic Conc %	Mass Conc %
Na 1s	Reg	1072.000	3.354	271643.2	1.685	22.990	5.37	6.42
Zn 2p 3/2	Reg	1022.000	4.215	39457.5	3.726	65.387	0.34	1.15
O 1s	Reg	532.000	3.146	2160109.2	0.780	15.999	62.07	51.64
Sn 3d	Reg	487.000	2.806	72232.6	7.875	118.744	0.20	1.23
Ca 2s	Reg	439.000	4.620	27369.2	1.022	40.078	0.57	1.18
C 1s	Reg	285.000	3.294	134277.9	0.278	12.011	9.24	5.77
Cl 2p	Reg	198.000	3.296	34055.4	0.891	35.460	0.69	1.26
Si 2p	Reg	103.000	2.901	395932.9	0.328	28.086	20.96	30.62
Hg 2p	Reg	49.000	2.628	5566.0	0.168	24.312	0.56	0.71
State : Angle Name : 120C uncoated pt.2								
Peak	Type	Position BE (eV)	FWHM (eV)	Raw Area (cps eV)	RSF	Atomic Mass	Atomic Conc %	Mass Conc %
Na 1s	Reg	1072.000	2.839	233028.9	1.685	22.990	4.86	5.88
Zn 2p 3/2	Reg	1022.000	3.132	30257.6	3.726	65.387	0.27	0.94
O 1s	Reg	533.000	3.052	1963258.4	0.780	15.999	59.74	50.29
Sn 3d	Reg	487.000	2.797	56463.7	7.875	118.744	0.16	1.03
Ca 2s	Reg	439.000	4.544	28610.5	1.022	40.078	0.62	1.32
C 1s	Reg	285.000	2.837	167025.8	0.278	12.011	12.13	7.67
Cl 2p	Reg	199.000	2.703	28477.8	0.891	35.460	0.61	1.13
Si 2p	Reg	103.000	2.903	371865.7	0.328	28.086	20.78	30.70
Hg 2p	Reg	50.000	3.510	7630.8	0.168	24.312	0.81	1.04

Table VII: Results of survey spectra of uncoated glass heated to 450°C.

State : Angle Name : 450C uncoated								
Peak	Type	Position BE (eV)	FWHM (eV)	Raw Area (cps eV)	RSF	Atomic Mass	Atomic Conc %	Mass Conc %
Na 1s	Reg	1071.500	2.823	434246.7	1.685	22.990	8.22	9.95
Zn 2p 3/2	Reg	1021.500	2.154	15320.1	3.726	65.387	0.13	0.43
O 1s	Reg	532.500	3.232	2232427.8	0.780	15.999	61.43	51.76
Sn 3d	Reg	486.500	2.635	46963.3	7.875	118.744	0.12	0.78
Ca 2s	Reg	438.500	3.577	43817.3	1.022	40.078	0.87	1.83
C 1s	Reg	285.500	3.025	141131.9	0.278	12.011	9.31	5.89
Cl 2p	Reg	1407.500	1.000	0.0	0.891	35.460	0.00	0.00
Si 2p	Reg	102.500	2.326	381545.7	0.328	28.086	19.34	28.60
Hg 2p	Reg	49.500	2.459	6081.2	0.168	24.312	0.59	0.75
State : Angle Name : 450 uncoated pt.2								
Peak	Type	Position BE (eV)	FWHM (eV)	Raw Area (cps eV)	RSF	Atomic Mass	Atomic Conc %	Mass Conc %
Na 1s	Reg	1071.500	2.829	343622.2	1.685	22.990	6.61	7.95
Zn 2p 3/2	Reg	1016.500	3.364	10932.4	3.726	65.387	0.09	0.31
O 1s	Reg	532.500	3.182	2252018.0	0.780	15.999	63.02	52.73
Sn 3d	Reg	487.500	2.781	52084.3	7.875	118.744	0.14	0.87
Ca 2s	Reg	438.500	4.315	32053.1	1.022	40.078	0.65	1.35
C 1s	Reg	285.500	3.080	113614.4	0.278	12.011	7.62	4.79
Cl 2p	Reg	1407.500	1.000	0.0	0.891	35.460	0.00	0.00
Si 2p	Reg	103.500	3.072	412420.0	0.328	28.086	21.26	31.23
Hg 2p	Reg	49.500	2.400	6167.1	0.168	24.312	0.61	0.77

Table VIII: Results of contact angle measurements. (*) One-pot coatings are formulated differently, see 3.1.2. (**) didn't slide off. (***) for aging, refer to Appendix A. All by sessile drop method with 10 μ l droplet. HP stands for hydrophobization.

SAMPLE TYPE	FOR- MULA- TION	SUB- STRATE	TEOS [wt%]	HCl [M]	AGING (***)	DIP NR	POST- TREAT- MENT [°C]	HP METHOD	WCA [°]	RA [°]	RADP [°]
GL030BO	0C	Glass	0	1	no	2	120	OTS	151 \pm 1	9 \pm 1	29 \pm 1
GL030CH	0C	Glass	0	1	no	2	450	HMDSO	145 \pm 4	13 \pm 0	20 \pm 3
GL110CO	3A	Glass	10	0.01	no	2	450	OTS	160 \pm 0	2 \pm 0	-
GL110COX1	3A	Glass	10	0.01	no	1	450	OTS	160 \pm 1	3 \pm 1	**
GL130B1	O1	Glass	9.8	*	no	2	120	One pot	149 \pm 0	18 \pm 3	56 \pm 7
GL130B1X1	O1	Glass	9.8	*	no	1	120	One pot	144 \pm 2	**	-
GL510B2	O52	Glass	5	*	no	2	120	One pot	140 \pm 1	**	-
GL510B3	O53	Glass	5	*	no	2	120	One pot	136 \pm 2	**	-
GL510B4	O54	Glass	5	*	no	2	120	One pot	137 \pm 3	**	-
GL510BO	1A	Glass	5	0.01	no	2	120	OTS	160 \pm 1	2 \pm 1	-
GL510CO	1A	Glass	5	0.01	no	2	450	OTS	160 \pm 0	3 \pm 1	-
GL524BO	1B	Glass	5	0.1	4	2	120	OTS	151 \pm 2	6 \pm 2	16 \pm 1
GL530BO	1C	Glass	5	1	no	2	120	OTS	149 \pm 3	11 \pm 3	22 \pm 13
GL530CH	1C	Glass	5	1	no	2	450	HMDSO	148 \pm 1	22 \pm 6	34 \pm 4
GL534BO	1C	Glass	5	1	4	2	120	OTS	149 \pm 1	6 \pm 2	23 \pm 5
GL710CO	2A	Glass	7.5	0.01	no	2	450	OTS	159 \pm 1	4 \pm 1	-
GL710COX1	2A	Glass	7.5	0.01	no	1	450	OTS	158 \pm 1	6 \pm 2	-
GL724BO	2B	Glass	7.5	0.1	4	2	120	OTS	151 \pm 1	4 \pm 0	13 \pm 1
GL730BO	2C	Glass	7.5	1	no	2	120	OTS	150 \pm 1	7 \pm 1	16 \pm 2
GL730CH	2C	Glass	7.5	1	no	2	450	HMDSO	149 \pm 1	15 \pm 2	32 \pm 2
GL734BO	2C	Glass	7.5	1	4	2	120	OTS	152 \pm 0	4 \pm 0	15 \pm 2
P1	-	SiOx 1 min	-	-	-	-	-	-	91 \pm 1	37 \pm 11	-
P1530CO	1C	SiOx 1 min	5	1	no	2	450	OTS	150 \pm 1	6 \pm 2	17 \pm 1
P1730CO	2C	SiOx 1 min	7.5	1	no	2	450	OTS	147 \pm 1	9 \pm 4	19 \pm 3
P2	-	SiOx 2 min	-	-	-	-	-	-	97 \pm 1	37 \pm 3	-
P2530CO	1C	SiOx 2 min	5	1	no	2	450	OTS	146 \pm 3	24 \pm 3	57 \pm 5
P2730CO	2C	SiOx 2 min	7.5	1	no	2	450	OTS	148 \pm 2	22 \pm 5	41 \pm 16
GL	-	-	-	-	-	-	-	-	11 \pm 1	20 \pm 1	-

Table IX: Results for tape peel tests. All samples were dipped two times. (*) for aging, refer to Appendix A. HP stands for hydrophobization.

SAMPLE TYPE	FORMULA-TION	SUBSTRATE	TEOS [wt%]	HCl [M]	AGING (*)	POST-TREAT-MENT [°C]	HP METHOD	PEEL FORCE [N]
GL110CO	3A	Glass	10	0.01	no	450	OTS	8.20±0.82
GL510CO	1A	Glass	5	0.01	no	450	OTS	2.09±0.22
GL520C	1B	Glass	5	0.1	no	450	-	2.35±0.12
GL524B	1B	Glass	5	0.1	4	120	-	1.54±0.02
GL524C	1B	Glass	5	0.1	4	450	-	3.22±0.12
GL524B	1B	Glass	5	0.1	A	120	-	1.54±0.02
GL524C	1B	Glass	5	0.1	A	450	-	2.57±0.12
GL530C	1C	Glass	5	1	no	450	-	3.01±0.32
GL534B	1C	Glass	5	1	4	120	-	1.54±0.02
GL534C	1C	Glass	5	1	4	450	-	2.92±0.12
GL534B	1C	Glass	5	1	A	120	-	2.12±0.12
GL534C	1C	Glass	5	1	A	450	-	3.63±0.12
GL710CO	2A	Glass	7.5	0.01	no	450	OTS	6.02±2.42
GL720C	2B	Glass	7.5	0.1	no	450	-	4.75±0.02
GL724B	2B	Glass	7.5	0.1	4	120	-	2.05±0.12
GL724C	2B	Glass	7.5	0.1	4	450	-	6.72±0.52
GL730C	2C	Glass	7.5	1	no	450	-	6.75±2.22
GL734B	2C	Glass	7.5	1	4	120	-	2.41±0.12
GL734C	2C	Glass	7.5	1	4	450	-	8.14±0.12
GL75AB	2D	Glass	7.5	0.55	A	120	-	4.61±0.22
GL75AC	2D	Glass	7.5	0.55	A	450	-	8.58±0.02

Table X: Sample table for freeze-thaw cycling test. Sample L and M were dipped once, all other samples were dipped two times. (*) Samples K1 and K2 are one-pot and are formulated differently, read in Section 3.1.2 of this thesis work. FTC stands for freeze-thaw cycles and FTS for freeze-thaw survival, see Section 3.2.3. Last column shows solar weighted transmittance after 15 freeze-thaw cycles.

SAMPLE TYPE	LABEL	SUB-STRATE	TEOS [wt%]	HCl [M]	POST-TREATMENT [°C]	HP METHOD	FTS 4 FTC	FTS 9 FTC	FTS 15 FTC	WCA 15 FTC [°]	RA 15 FTC [°]	TSW 15 FTC [%]
GL030CH	A1	Glass	0	1	450	HMDSO	50%	33%	10%	119±29	21	71.7
GL030CH	A2	Glass	0	1	450	HMDSO	100%	67%	30%	142±25	19±4	88.1
GL530CH	B1	Glass	5	1	450	HMDSO	100%	100%	70%	99±20	22±6	79.5
GL530CH	B2	Glass	5	1	450	HMDSO	100%	80%	100%	137±30	30±8	83.0
GL730CH	C1	Glass	7.5	1	450	HMDSO	100%	100%	100%	122±31	20±3	88.2
GL730CH	C2	Glass	7.5	1	450	HMDSO	33%	100%	50%	133±25	37±10	75.5
GL530BO	D1	Glass	5	1	120	OTS	33%	60%	40%	126±26	19±26	85.2
GL530BO	D2	Glass	5	1	120	OTS	100%	60%	56%	148±3	47±13	80.7
GL030BO	E1	Glass	0	1	120	OTS	100%	67%	30%	137±21	30±40	76.4
GL030BO	E2	Glass	0	1	120	OTS	100%	67%	70%	140±26	9±9	71.8
GL730BO	F1	Glass	7.5	1	120	OTS	100%	50%	70%	151±3	18±19	83.0
GL730BO	F2	Glass	7.5	1	120	OTS	100%	100%	80%	110±26	17±29	86.7
P1530CO	G	SiO _x 1 m	5	1	450	OTS	100%	80%	80%	148±13	19±26	87.6
P1730CO	H	SiO _x 1 m	7.5	1	450	OTS	100%	80%	70%	147±23	10±12	85.2
P2530CO	I	SiO _x 2 m	5	1	450	OTS	100%	67%	50%	154±3	18±3	84.2
P2730CO	J	SiO _x 2 m	7.5	1	450	OTS	100%	60%	70%	143±18	28±22	87.7
GL130B1	K1	Glass	9.8	*	120	One-pot	100%	33%	40%	149±19	18±5	62.3
GL130B1	K2	Glass	9.8	*	120	One-pot	33%	67%	40%	139±33	31±17	68.1
GL710COX1	L	Glass	7.5	0.01	450	OTS	67%	50%	20%	134±25	40±32	81.5
GL110COX1	M	Glass	10	0.01	450	OTS	100%	67%	40%	150±7	8±7	82.5